Analysis and characterization of the nonlinear optical properties of plasmonic metamaterials

Barbosa Neira, Andres David

Awarding institution:
King's College London

Analysis and characterization of the nonlinear optical properties of plasmonic metamaterials

A dissertation presented

by

ANDRES DAVID BARBOSA NEIRA

for the degree of

Doctor of Philosophy (PhD)

KING'S COLLEGE LONDON

London, United Kingdom

September 2014

Abstract:

Metamaterials are materials whose optical properties can be designed through the accurate engineering of their structure on the subwavelength scale. They have enabled the discovery and study of a variety of interesting new optical properties not normally present in materials found in nature. Furthermore, by designing the local electromagnetic field distributions of such metamaterials, it is possible to engineer not only their linear optical properties but also their nonlinear response, which is fundamental for the development of nonlinear and active nanophotonics for all-optical information processing. In this thesis I will show that plasmonic metamaterials based on metallic nanorod arrays can be designed to have strong third-order nonlinear optical response originating from the nonlinearity of the plasmonic component of the metamaterial, allowing nonlinear processes to be more energy efficient and highly integrated. The nonlinearity will be experimentally determined through the z-scan technique and explained by numerical modeling in both effective medium and full-vectorial simulations. Enhancements of about 50 times for the nonlinear absorption and about 10 times for the nonlinear refraction are observed compared to a smooth metal film. Furthermore, the properties of waveguides comprised of the nanorod metamaterial are studied and the possibility of their integration in conventional Si photonic waveguides is demonstrated. In this context, two all-optical modulators using plasmonic metamaterials are designed, operating in the hyperbolic and epsilon near-zero regimes. Both designs are highly integrated and energy efficient having footprints of 300x440x600 nm^3 and 300x180x340 nm^3 with an energy consumption of 3.7 pJ/bit and 0.6pJ/bit respectively. The obtained results show great opportunities for nonlinear metamaterials in nanophotonic applications.

Acknowledgements

Firstly I would like to thank King's College London for having awarded me the King's overseas research studentship whose support has been fundamental during my PhD.

Secondly I would like to thank my supervisor Anatoly Zayats for having given me the opportunity to work with him on these amazing projects that have strongly enhanced incredibly my understanding of the behavior of light. I thank him together with Gregory Wurtz for their patience with me during the discussions.

I would like also to acknowledge Nicolas Olivier for his patience in teaching me the experimental equipment used particularly the femtosecond laser and the optical parametric amplifier, which have been fundamental in my experiments.

Additionally I would like to acknowledge Mazhar Nasir and Wayne Dickson for having provided me with the plasmonic metamaterial (gold nanorod array) samples that I optically characterize.

I would like also to thank Cillian Mcpolin and Silvia Peruch for being such good colleagues and friends during this trip.

Finally I would like to thank my family especially my mother Luz Neira, who have supported me since the beginning. She has given me the conviction to arrive where I am.

TABLE OF CONTENTS

Chapter 1: Introduction

Moore's law is the observation of the doubling of transistors' number approximately every two years, in integrated circuits. Thus the capabilities of many electronic devices are linked to this law in terms of: processing speed, memory capability, number and size of pixels, etc. [1] Furthermore, as new applications have been developed over time for the use of these capabilities, the demand for them has also been following Moore's law, and the need for the increase of them grows every year in the market. However, it has been predicted that the trend imposed by Moore's law will reach its limit in the following decade as the amount of transistors needed will require the development of transistors at the molecular scale (less than 5 nm) where signal degrading effects such as quantum tunneling become important [2]. Additionally, as a consequence of the RC (resistance-capacitive) delay of the electric connections in current integrated circuits, the maximum switching speed of the signal is limited to few tens of GHz [3]. Nevertheless, in order to supply the market's demand, Moore's law must continue and this has lead to research in alternative technologies, which could overcome the limits of current technology. There are several alternative technologies that have risen to the challenge although three of them have been developed greatly in the last decade and are strong candidates to take over Moore's Law. The first one is called spintronics, which relies on the switching of the electron spin. This technology has shown great signal speeds (in the order of hundreds of GHz) and low energy consumption (tens of aJ) [4].

The second one consists of the use of high electron-mobility materials such as graphene. In this case, the electrons and holes at the Dirac point (the crossing point of the energy dispersion curves) can be regarded as massless since the energy dispersion is linear[5]. Although the zero density of states at the Dirac point makes the electronic conductivity

low, the Fermi level can be changed by doping the material. Thus obtaining electron mobility only limited by the scattering with the substrate phonons. Indeed a limit in electron mobility of 40000 $cm^2.V^{-1}s^{-1}$ was measured for graphene on SiO_2 [6]. Consequently, the high conductivity of graphene provides a reduced delay in the electric interconnection [7]. However there are several drawbacks in the use of graphene such as the difficulty in its massive production and the lack of band gap, required for the construction of graphene-based switches (transistors). Therefore it is unlikely that graphene will be part of high-performance integrated circuits within the next decade [8] although several advances have been made using graphene nanoribbons, which do have a band gap [9]. Nevertheless, both of these technologies rely still in the use of electrical interconnections and thus their switching speed is still limited by the delay imposed by them.

The third alternative is the use of photonics, specifically silicon photonics. In this case the information will travel as light or in other words, as photons instead of electrons. Thus the signal is sent through optical interconnections, which do not have RC delay. This technology has already been used for the development of high speed, low power consumption optical chips by companies such as Intel and IBM able to achieve transfer bit rates in the order of 1 Tbps (Terabits per second) [10, 11]. Furthermore it has also been shown that old fabrications techniques used for electronic circuits can also be used in the development of optical chips as the materials required are similar (i.e. Silicon), making the development of optical chips cost effective [12]. However, there are some limits that need to be overcome for this technology to have a strong advantage against current electronic chips.

The first limit, called the diffraction limit, states that light cannot be confined in regions smaller than the wavelength of light (λ). In silicon photonics, the working wavelength of preference is 1.55 μm since the intrinsic absorption of both SiO_2 and Si is much lower [13]. At this wavelength, the refractive index of silicon is large (n=3.48), and light can be guided through single mode silicon waveguides having size as small as λ/n~450 nm. However light cannot be guided using waveguides with size below this limit because of diffraction. This imposes a fundamental limit in the integration of silicon based photonic devices.

The second is the limit in the modulation speed of an optical signal. Although optical signals can support a large signal modulation bandwidth, to achieve maximum speed the modulation of them has until now been done using electro-optical modulation. Typically a component setup using this type of modulation consists of an ultrafast photodiode, which converts the input optical signal to an electric signal and an optical circuit (typically a ring resonator) composed of a material whose refractive index changes with an electric field. Therefore the output electric signal of the photodiode is used to modulate the optical signal travelling through the optical circuit [14]. However there are two main drawbacks in the use of electro-optical modulation. Firstly, its speed depends on the RC delay time of the interconnection driving the modulating electric field. Although in general this interconnection is shorter than in the case of electronic circuits as it only has to connect the photodiode to the modulator, still the maximum speed of modulation is still limited by the RC delay and therefore modulation speed ranges in the order of hundreds of GHz [14, 15]. Secondly, the area required for the integration of all the required components is in the order of ~100 μm^2 [14]. This value is orders of magnitude larger than the integration of current electronic components and

therefore limits strongly the total number of bits per second handled by the total optoelectronic chip.

An obvious alternative that could solve the first and possibly the second problems of electro-optical modulation would be all-optical modulation. In this case one light beam will interact with a second light beam, modulating it and therefore the conversion from optical to electric signal is not needed. This interaction occurs through a material called nonlinear optical material or nonlinear material, whose refractive index (and permittivity) varies according to the intensity of light. Although all materials are generally nonlinear, usually this variation of their refractive index is very weak and an appreciable change of it requires beam intensities larger than 1 MW/cm^2 at the material's surface [16]. Therefore the power consumption of any photonic circuit using this interaction will be extremely large and cannot be sustained in an integrated and compact fashion.

Plasmonics is an alternative to overcome these limits. It is based on the coupling of light (or photons) to the oscillations of the electrons' plasma of metals (plasmons) [17]. There are two valuable characteristics that renders plasmons fundamental to solve the problems of current technology. First, plasmons can be highly confined in regions in the order of ~20 nm, below the diffraction limit. This allows them to be used for the transport of light signals in highly integrated systems [18, 19]. Second, plasmons have high field intensity, allowing them to produce an increased nonlinear optical response with less energy. A clear example of this, is the case of gold nanoparticles (or nanospheres), whose third order nonlinear coefficient is 4 orders of magnitude larger than that of bulk gold [16]. Additionally, this behavior has also been characterized

through the study of the nonlinear optical properties of metamaterials, which are materials exhibiting properties not found in nature like negative refraction, cloaking, etc. These properties are not a consequence of the materials composing the metamaterial, but of the accurately designed patterning of them [20, 21]. Plasmonic metamaterials, a specific kind of metamaterials, are designed using metals and therefore take advantage of the great confinement of plasmons to produce this variety of properties. Therefore, thanks to the presence of plasmons in plasmonic metamaterials, their nonlinear optical variation is strongly enhanced and additionally, it has been shown that it can be tuned in wavelength through the design of the metamaterial structure [22]. Furthermore, metals have inherent ultrafast nonlinear properties. These properties are attributed to the creation through optical excitation of a hot electron gas in the conduction band, which afterwards will cool down through electron-phonon scattering within a time interval varying between hundreds of femtoseconds to few picoseconds depending on the structure [23]. Consequently, plasmonic metamaterials are fundamental for the development of integrated all-optical modulation as through their engineering it is possible to tune their optical nonlinearity which additionally is inherently ultrafast [24]

In this thesis, I will theoretically and experimentally characterize the intensity-dependent nonlinearity of plasmonic metamaterials based on metallic nanorod arrays. These metallic nanorod arrays are fabricated following a electro-deposition technique detailed in [25]. Furthermore I will propose two designs of all-optical modulators taking advantage of their nonlinearity. In the second chapter, I will introduce the theory for the description of the linear and nonlinear optical properties of metals and plasmonic metamaterials based on metallic nanorod arrays. It will be shown that the inherent

ultrafast nonlinearity of metals will be the main component driving the nonlinear optical response of plasmonic metamaterials. In the third chapter, I will describe the Z-Scan technique, which is used to the experimental characterization of the nonlinearity of these materials. Additionally as an example, I will report the results obtained through this technique for the nonlinear optical properties of a smooth gold film. These will be compared later with the results obtained for the plasmonic metamaterial. In the fourth chapter, I will characterize both theoretically and experimentally using the tools developed in the previous chapters, the nonlinearity of a plasmonic metamaterial based on gold nanorod array. The results will show the enhancement of its optical nonlinearity with respect to that of a smooth film as a consequence of the metamaterial structure. In the fifth chapter, I will introduce the first design of an all-optical modulator, which takes advantage of the hyperbolic dispersion and high confinement present in plasmonic metamaterial-based waveguides. Finally in the sixth chapter I will introduce the second design of an all-optical modulator based on the ENZ (epsilon-near zero) condition of the metamaterial which allows the creation of highly reflective and highly optically nonlinear thin layers. These layers can be used for the design of a resonant nonlinear optical cavity.

References

[1] G. E. Moore, "Cramming More Components Onto Integrated Circuits," *Proceedings of the IEEE,* vol. 86, pp. 82-85, 1998.

[2] R. W. Keyes, "The Impact of Moore's Law," *Solid-State Circuits Society Newsletter, IEEE,* vol. 11, pp. 25-27, 2006.

[3] D. A. B. Miller and H. M. Ozaktas, "Limit to the Bit-Rate Capacity of Electrical Interconnects from the Aspect Ratio of the System Architecture," *Journal of Parallel and Distributed Computing,* vol. 41, pp. 42-52, 1997.

[4] D. E. Nikonov and I. A. Young, "Overview of Beyond-CMOS Devices and a Uniform Methodology for Their Benchmarking," *Proceedings of the IEEE,* vol. 101, pp. 2498-2533, 2013.

[5] G. W. Semenoff, "Condensed-Matter Simulation of a Three-Dimensional Anomaly," *Physical Review Letters,* vol. 53, pp. 2449-2452, 1984.

[6] J.-H. Chen, C. Jang, S. Xiao, M. Ishigami, and M. S. Fuhrer, "Intrinsic and extrinsic performance limits of graphene devices on SiO2," *Nat Nano,* vol. 3, pp. 206-209, 2008.

[7] A. K. Geim and K. S. Novoselov, "The rise of graphene," *Nat Mater,* vol. 6, pp. 183-191, 2007.

[8] K. S. Novoselov, V. I. Falko, L. Colombo, P. R. Gellert, M. G. Schwab, and K. Kim, "A roadmap for graphene," *Nature,* vol. 490, pp. 192-200, 2012.

[9] J. J. Palacios, "Graphene nanoribbons: Electrons go ballistic," *Nat Phys,* vol. 10, pp. 182-183,.

[10] C. Vu. (2012) Made in IBM Labs: Holey Optochip First to Transfer One Trillion Bits of Information per Second Using the Power of Light. *IBM press release*. Available: http://www-03.ibm.com/press/us/en/pressrelease/37095.wss

[11] T. Simonite. (2013) Intel's Laser Chips Could Make Data Centers Run Better. *MIT Technology Review*. Available: http://www.technologyreview.com/news/518941/intels-laser-chips-could-make-data-centers-run-better/

[12] J. M. Shainline, J. S. Orcutt, M. T. Wade, K. Nammari, B. Moss, M. Georgas, *et al*., "Depletion-mode carrier-plasma optical modulator in zero-change advanced CMOS," *Optics Letters,* vol. 38, pp. 2657-2659, 2013.

[13] M. Lipson, "Guiding, Modulating, and Emitting Light on Silicon-Challenges and Opportunities," *Journal of Lightwave Technology,* vol. 23, p. 4222, 2005.

[14] D. A. B. Miller, "Device Requirements for Optical Interconnects to Silicon Chips," *Proceedings of the IEEE,* vol. 97, pp. 1166-1185, 2009.

[15] S. Kodama, T. Yoshimatsu, and H. Ito, "500 Gbit/s optical gate monolithically integrating photodiode and electroabsorption modulator," *Electronics Letters,* vol. 40, pp. 555-556, 2004.

[16] R. W. Boyd, *Nonlinear optics*, 3rd ed. Amsterdam ; Boston: Academic Press, 2008.

[17] S. A. Maier, *Plasmonics : fundamentals and applications*. New York: Springer, 2007.

[18] A. V. Krasavin and A. V. Zayats, "Silicon-based plasmonic waveguides," *Optics Express,* vol. 18, pp. 11791-11799, 2010.

[19] A. V. Krasavin, S. Randhawa, J.-S. Bouillard, J. Renger, R. Quidant, and A. V. Zayats, "Optically-programmable nonlinear photonic component for dielectric-loaded plasmonic circuitry," *Optics Express,* vol. 19, pp. 25222-25229, 2011.

[20] A. Alù and N. Engheta, "Achieving transparency with plasmonic and metamaterial coatings," *Physical Review E,* vol. 72, p. 016623, 2005.

[21] J. B. Pendry, "Negative Refraction Makes a Perfect Lens," *Physical Review Letters,* vol. 85, pp. 3966-3969, 2000.

[22] M. Kauranen and A. V. Zayats, "Nonlinear plasmonics," *Nat Photon,* vol. 6, pp. 737-748, 2012.

[23] L. Jiang and H.-L. Tsai, "Improved Two-Temperature Model and Its Application in Ultrashort Laser Heating of Metal Films," *Journal of Heat Transfer,* vol. 127, pp. 1167-1173, 2005.

[24] G. A. Wurtz, Pollard R, Hendren W, G. P. Wiederrecht, D. J. Gosztola, V. A. Podolskiy, *et al*., "Designed ultrafast optical nonlinearity in a plasmonic nanorod metamaterial enhanced by nonlocality," *Nature Nanotechnology,* vol. 6, pp. 107-111, 2011.

[25] R. Atkinson, W. R. Hendren, G. A. Wurtz, W. Dickson, A. V. Zayats, P. Evans, *et al*., "Anisotropic optical properties of arrays of gold nanorods embedded in alumina," *Physical Review B,* vol. 73, p. 235402, 2006.

Chapter 2: Theory of the linear and the nonlinear optical properties of metals and plasmonic metamaterials

In this chapter I will describe the theory used for the modeling of the linear and nonlinear optical properties of plasmonic metamaterials. Firstly, I will give a brief introduction to nonlinear optics and its development in the last decades. Some nonlinear optical effects will be described in particular the Kerr effect corresponding to the change in the permittivity of a material with the intensity of light. Secondly, I will describe the permittivity of metals, main component of plasmonic metamaterials, through the random phase approximation. Within this theory, both interband and intraband electron transitions are taken into account allowing a complete description of the metal permittivity in a broad wavelength range. The resulting permittivity is dependent on the electron scattering, which can be increased through illumination with high intensity light. This behavior will be analyzed through the dependence of the electron scattering on the temperature of the electron gas inside the metal. Thirdly, I will describe the optical properties of metamaterials based on nanorod array through the Maxwell-Garnett theory, which allows the definition of an effective permittivity tensor dependent on the permittivity of the metamaterial compounds. Finally, I will show a self-consistent method to determine theoretically the nonlinear optical properties of metals and plasmonic metamaterials for further comparison with the experimental results obtained.

2.1 What is nonlinear optics?:

Nonlinear optical materials are those materials whose optical properties depend on the intensity of light present. All materials have nonlinear optical properties, although generally, the visualization of these properties require a high light intensity for the majority of materials [1]. An example of nonlinear materials is fluorescent materials whose interaction with light allows them to produce additional colors through a process called spontaneous emission of radiation [2]. Also LASERs take advantage of the nonlinear optical properties of a material (gain-material) to amplify the intensity of light through a process called stimulated emission of radiation. Their invention and development has allowed the possibility to reach high light intensities allowing in the last decades, the study of the nonlinear optical properties for different materials, increasing the understanding of the ongoing processes occurring when light interacts with matter [3, 4]. Nonlinear optical properties are related to the nonlinear dependence of the material's polarization to the electric field amplitude ($E(t)$). Therefore the polarization can be expanded as a power series of $E(t)$:

$$P(E(t)) = \varepsilon_0(\chi^{(1)}E(t) + \chi^{(2)}E(t)^2 + \chi^{(3)}E(t)^3 + ...) \tag{2.1}$$

where ε_0 is the permittivity of the vacuum [1]. The first term ($\varepsilon_0\chi^{(1)}E(t)$) is the linear polarization, corresponding to the conventional optical response at low light intensity and $\chi^{(1)}$ is the linear susceptibility. The second term corresponds to the second order nonlinear polarization which leads to two different kinds of nonlinear effects. These effects can be analyzed easily by assuming an electric field harmonic in time for an incident electromagnetic wave represented by [5]:

$$E(t) = E_0 e^{-i\omega t} + c.c \tag{2.2}$$

(where ω is the frequency related to the propagation constant k and the speed of light c through $\omega = ck$ and c.c means the complex conjugate), and replacing it in the second term of equation (2.1) obtaining:

$$\varepsilon_0 \chi^{(2)} E(t)^2 = 2\varepsilon_0 \chi^{(2)} E_0 E_0^{\ *} + (\varepsilon_0 \chi^{(2)} E_0^2 e^{-i2\omega t} + \text{c.c}) \tag{2.3}$$

Equation (2.3) is composed of two terms; a zero frequency term and a 2ω frequency term. The latter corresponds to the generation of radiation with two times the frequency of the incident wave and it is called second harmonic generation (SHG). The zero frequency term does not contribute to generation of radiation since its second derivative over time vanishes. However it is related to a nonlinear effect called optical rectification, corresponding to the creation of a static electric field across the material [5].

A similar analysis can be done for the third term in equation (2.1). In this case we obtain:

$$\varepsilon_0 \chi^{(3)} E(t)^3 = \varepsilon_0 \chi^{(3)} e^{-i3\omega t} + 3\varepsilon_0 \chi^{(3)} E_0^{\ 2} E_0^* e^{-i\omega t} + c.c \tag{2.4}$$

The first term corresponds to the third harmonic generation (THG) because this term has a component at 3ω . The second term has the same frequency of the incident wave; this allows us to define an effective susceptibility, which is dependent on the magnitude of the electric field. Replacing equation (2.2) in equation (2.1) and taking into account only terms in first and third order dependent on E_0 , the resulting polarization from those terms is:

$$P_{res}(t) = (\chi^{(1)} + 3\varepsilon_0 \chi^{(3)} \left|E_0\right|^2)(E_0 e^{-i\omega t} + \text{c.c}) \tag{2.5}$$

With an effective susceptibility:

$$\chi_{eff} = \chi^{(1)} + 3\varepsilon_0 \chi^{(3)} \left|E_0\right|^2 \tag{2.6}$$

This effective susceptibility can also be written in terms of the time-averaged intensity of an optical field, which is related to the magnitude of the electric field through

$$I = 2\,\mathrm{Re}(n_0)\varepsilon_0 c\left|E_0\right|^2 \tag{2.7}$$

with $n_0 = (1+\chi^{(1)})^{1/2}$ being the linear refractive index of the material which can be complex in the case of metals, and c is the speed of light. Therefore the effect generated by this term corresponds to an intensity dependent variation in the phase and amplitude of the wave propagating inside the nonlinear material. This is known as Kerr effect. Since these variations are directly related to a variation of the complex refractive index of the material it is very useful to define an intensity dependent refractive index ($n(I)$)

$$n(I) = n_0 + n_2 I \tag{2.8}$$

Where n_0 and n_2 are the complex linear and nonlinear refractive indexes respectively and I is the intensity of the beam inside the material. Using equations (2.6-2.8) it is possible to show that n_2 is related to $\chi^{(3)}$. Since $n(I)$ is related to the effective susceptibility through:

$$n(I)^2 = 1 + \chi_{eff} \tag{2.9}$$

it is possible to replace equation (2.6) and equation (2.8) in equation (2.9), obtaining:

$$(n_0 + n_2 I)^2 = 1 + \chi^{(1)} + 3\chi^{(3)}\left|E_0\right|^2 \tag{2.10}$$

Expanding the term in the left, using equation (2.7) and keeping to terms up to first order in $\left|E_0\right|^2$, we obtain:

$$n_0{}^2 + 2n_0 n_2\,\mathrm{Re}(n_0)\varepsilon_0 c\left|E_0\right|^2 = 1 + \chi^{(1)} + 3\chi^{(3)}\left|E_0\right|^2 \tag{2.11}$$

Therefore the linear and nonlinear refractive index coefficients can be related to $\chi^{(1)}$ and $\chi^{(3)}$ through:

$$n_0 = (1+\chi^{(1)})^{1/2}$$
$$n_2 = \frac{3\chi^{(3)}}{4n_0\,\mathrm{Re}(n_0)\varepsilon_0 c} \tag{2.12}$$

This thesis will be focused on the analysis and measurement of the intrinsic Kerr effect of metallic nanostructures. In the following section I will provide the theory for the understanding of this Kerr effect and in the next chapter I will introduce the z-scan technique, which allows the measurement of the real and imaginary part of n_2 .

As a final remark, it is worth mentioning that if the optical field incident to the nonlinear material is composed of two or more frequencies, it is possible to achieve the generation of additional optical waves corresponding to the sum and difference between these frequencies, this effect is known as wave mixing [1].

2.2 The intensity-dependent refractive index of metals

Electrons inside a material interact through a Coulomb potential with the ion cores. A consequence of this interaction is that electrons can only have certain energy values. These energy values are separated in different energy bands. When an electron is provided with additional energy, this energy allows the change of its energy value. If the resultant energy value corresponds to a value within the same band, it is said that the electron performed an intraband transition, if it corresponds to a different band then it performed an interband transition [6]. Light can excite the two kinds of transitions depending on the photon energy, which is related to the wave angular frequency through $E = \hbar\omega$, where $\hbar$ is the reduced Planck constant related to the Planck constant through $\hbar = h/2\pi$. In metals, electrons occupy energy bands up to a band called conduction band, where the electrons can barely feel the coulomb potential of the ion cores and can move almost as if they were free particles. Therefore intraband transitions

in this band can readily be excited optically even with low photon energies. However if the photon energy is large enough to overcome the energy gap between the conduction band and the band below called valence band (See Figure 2.1), an interband transition can be excited.

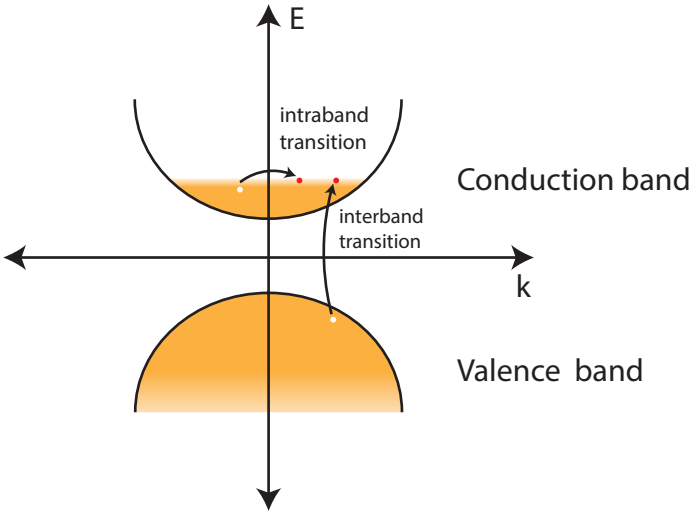

Figure 2.1 Graphical representation of interband and intraband transitions. The orange filling represents the states filled by electrons, white circles represent the creation of holes through the optical excitation of electrons.

In this context, the frequency dependent susceptibility of a metal depends on both intraband and interband transitions. The random phase approximation (RPA) allows the theoretical description of the dynamic properties of an electron gas which takes into account both interband and intraband transitions and the derivation of a total permittivity (related to the susceptibility through $\varepsilon(\omega)=1+\chi(\omega)$) which is [6]:

$$\varepsilon(\omega)=\varepsilon(\omega)_{\text{intra}}+\varepsilon(\omega)_{\text{inter}} \tag{2.13}$$

with $\varepsilon(\omega)_{\text{intra}}$ being the permittivity only dependent on intraband transitions and $\varepsilon(\omega)_{\text{inter}}$, the permittivity only dependent on interband transitions. Furthermore it can be shown within this approximation that the intraband transition term is [7]:

$$\varepsilon_{\text{intra}}(\omega)=\varepsilon_{\infty}-\frac{\omega_p^{\,2}}{\omega(\omega+i\gamma_{\text{intra}})} \tag{2.14}$$

where $\omega_p = \sqrt{4\pi e^2 N / m}$ is the plasma frequency of the electron gas related to the electron charge (e) electron mass (m) and the electron density in the metal N, ε_∞ is the high-frequency limit of the permittivity, and γ_{intra} is the scattering cross-section corresponding to the inverse of the energy decay time of electrons excited through interband transitions. Additionally it can also be shown that the interband transition term is [7]:

$$\varepsilon_{\text{inter}}(\omega) = K\int_0^\infty \frac{\sqrt{\hbar x - E_g}}{x}(1 - f(x,T_e))\frac{({\gamma_{\text{inter}}}^2 - \omega^2 + x^2) + 2i\omega\gamma_{\text{inter}}}{({\gamma_{\text{inter}}}^2 - \omega^2 + x^2)^2 + 4{\gamma_{\text{inter}}}^2\omega^2}dx \qquad (2.15)$$

where $K = 8\mu^2 e^2 m\sqrt{2m} / \pi\hbar^3 m^2$ with μ being the dipole moment of interband transitions supposed to be wave vector independent and m the electron mass, E_g is the energy gap between the valence and the conduction band, $f(x,T_e)$ is the Fermi-Dirac distribution for the electrons at an equilibrium temperature T_e and depends on the metal interband energy transition (from the valence band to the top of the conduction band), and γ_{inter} is the interband scattering cross-section corresponding to electrons excited through interband transitions.

The energy decay of the electrons excited through interband and intraband transitions, depends mainly on collisions with the lattice phonons and other electrons. These can be visualized as a gas of particles having temperatures T_L and T_e respectively. The temperatures are proportional to the particles' velocity, which through momentum conservation is related to the energy decay caused by collisions of a particle travelling within the gas. Thus the expressions for the scattering cross-sections are a sum of the scattering cross-section contributions of electrons and phonons, which are dependent on T_L and T_e respectively. These expressions are:

$$\gamma_{\text{intra}}(T_{L,}T_e) = a_{\text{intra}}\gamma_{ph-e}(T_L) + b_{\text{intra}}(4\pi^2(k_\beta T_e)^2 + (\hbar\omega)^2)$$
$$\gamma_{\text{inter}}(T_{L,}T_e) = a_{\text{inter}}\gamma_{ph-e}(T_L) + b_{\text{inter}}\frac{(\pi^2(k_\beta T_e)^2 + (E_f - \hbar\omega)^2)}{1+\exp((E_f - \hbar\omega)/k_\beta T)} \quad (2.16)$$

The derivation of these formulae is beyond the scope of this thesis but can be found in great detail in [6, 8]. The term $\gamma_{ph-e}(T_L)$ corresponds to the electron-phonon scattering, which according to [9] is:

$$\gamma_{ph-e}(T_L) = \frac{2}{5} + 4\left(\frac{T_L}{\theta}\right)^5 \int_0^{\theta/T_L} \frac{x^4}{e^x - 1}dx \quad (2.17)$$

The second term in the right hand side of equations (2.16) corresponds to the electron-electron scattering, which in the case of interband transitions depends on the Fermi level energy E_f. Furthermore the constants a_{intra}, a_{inter}, b_{intra} and b_{inter} are free parameters used to fit the optical response of a specific metal at room temperature (300K).

At thermal equilibrium both T_L and T_e are equal. However under optical excitation electrons react almost instantaneously to the optical field (~0.1fs) creating an imbalance between these two temperatures and thus a modification in the optical properties of the metals. This imbalance further disappears as a consequence of electron-phonon coupling. This process is understood through the two-temperature model [10]. This model relates T_L and T_e through the following equations:

$$C_e T_e \frac{\partial T_e}{\partial t} = \nabla\cdot(K_e \nabla T_e) - g(T_e - T_L) + \omega_0 \,\text{Im}(\varepsilon)\langle E(r,t)\cdot E(r,t)\rangle$$
$$C_L \frac{\partial T_L}{\partial t} = g(T_e - T_L) \quad (2.18)$$

where $C_e = 67.96\ J/m^3K^2$ is the heat capacity of electrons, $g = 2\times10^{16} W/m^3K$ is a constant related to the coupling between electrons and phonons, $\langle E(r,t)\cdot E(r,t)\rangle$ is the time averaged electric field, $K_e = K_{e0}T_e/T_L$ is the electron heat diffusion with

$K_{e0} = 318 W/mK$ and C_L is the heat capacity for a specific metal. A consequence of the first of equations (2.18) is that if we neglect the electron heat diffusion and the electron phonon coupling, the electron temperature rises following the optical power corresponding to the last term in this equation. This corresponds to the instantaneous response of the electron gas to the optical field. In this case the first of equations (2.18) becomes:

$$C_e T_e \frac{\partial T_e}{\partial t} = \omega_0 \,\mathrm{Im}(\varepsilon)\langle E(r,t)\cdot E(r,t)\rangle \tag{2.19}$$

Using this equation the energy absorbed by the electrons from the optical power can be calculated:

$$\frac{1}{2} C_e T_e^{\,2} = \int \omega_0 \,\mathrm{Im}(\varepsilon)\langle E(r,t)\cdot E(r,t)\rangle dt = E_{abs}[J/m^3] \tag{2.20}$$

If the electron phonon coupling and the electron heat diffusion are now taken into account, the optical energy absorbed by the electrons will be transmitted to the phonons. The effect of these contributions can be understood examining two cases. In the case of a bulk metal this energy will be spread widely over the whole material through electron heat diffusion because of the high exponentially-decaying temperature gradient imposed by the optical field. In the case of a smooth film of few tens of nanometres, this gradient will vanish as a consequence of the almost constant distribution of the optical field over the film and the electron temperature decays through electron-phonon coupling.

Figure 2.2 shows the decay over time of the electron temperature at the surface of a metal for both bulk metal (d=∞) and smooth film (d=20 nm) assuming a starting electron temperature of 2500 K achieved through an ultrashort pulse (<100 fs). Indeed in the case of bulk metal the relaxation time of the electron temperature is in the order of few hundreds of femtoseconds as a result of the strong temperature gradient whereas the relaxation time in the smooth film follows a linear decay as a consequence of its

strong dependence with the electron-phonon coupling. The slope of the linear time decay can also be derived through the first of equations (2.18) neglecting the contribution from the diffusivity and assuming $T_L << T_e$, which is the case some femtoseconds after the excitation. Therefore the slope of the decay is $-g/C_e$ and in this case the decay time is $\sim C_e / g(2500-300) = 7.47\,ps$

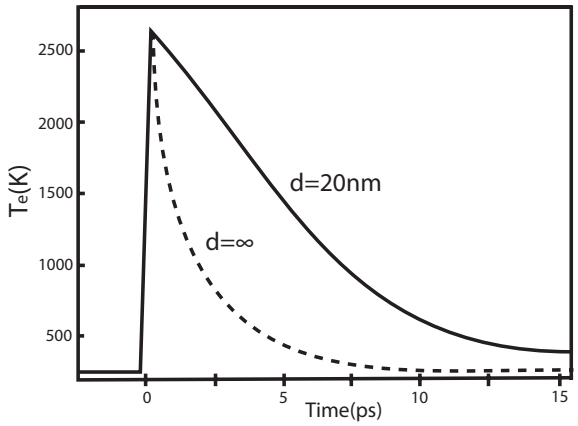

Figure 2.2. Electron temperature at the metal surface computed using equations (2.18) for the case of a thin film of 20 nm and bulk metal (d=∞). The equations were solved numerically by finite time domain technique using matlab.

In this thesis the properties of plasmonic metamaterials based on gold will be analysed. Therefore the model defined via equations (2.13-2.17) is used to fit the well-known experimental data for the real and imaginary part of the permittivity of gold. Figure 2.3 shows a comparison of our model fitting with the values measured by Johnson and Christy [11], and Pallik [12]. Table 2.1 shows the values used for the respective constants of equations (2.13-2.17). While our model presents some discrepancies fitting especially Pallik data in the ultraviolet where an additional interband transition is present, for wavelengths larger than 500 nm, it fits appropriately. Since this is the wavelength range for which the numerical analysis and experiments are realized in this thesis, our model is very reliable.

To summarize, the dependence of the metal permittivity to the electron and phonon temperatures, reveals the inherent Kerr effect of metals because electron and phonon temperatures can be modified through the optical intensity.

Constant	**Value**	**Units**
Θ(Debye temperature)	170	K
k_b(Boltzmann constant)	8.61×10^{-5}	eV/K
h(Planck constant)	4.136×10^{15}	eV/Hz
b_{intra}	0.0827/h	Hz/eV^2
a_{intra}	0.0125/h	Hz
b_{inter}	0.7/h	Hz/eV^2
a_{inter}	0.15/h	Hz
E_f (interband transition energy)	2.4	eV
E_g (band gap energy Au)	1.98	eV
K	1.2695×10^{32}	
ε_∞	1	
ω_p	2.168×10^{15}	Hz

Table 2.1. Constants for the equations (2.13-2.17) to model the permittivity of gold. Both electron and lattice temperature are assumed to be 300K

Furthermore it has been shown that the almost instantaneous response of the electrons to the optical field allows an ultrafast modification of the optical properties whose relaxation time is strongly dependent on the metal structure. Since this nonlinear behaviour is dependent on $\mathrm{Im}(\varepsilon)\langle E(r,t)\cdot E(r,t)\rangle$, electron and phonon temperatures, equations (2.18) must be solved through a self-consistent method together with Maxwell's equations. This method will be addressed in chapter 4 when I will analyse the modelling of the nonlinear properties of a plasmonic metamaterial based on gold nanorod array.

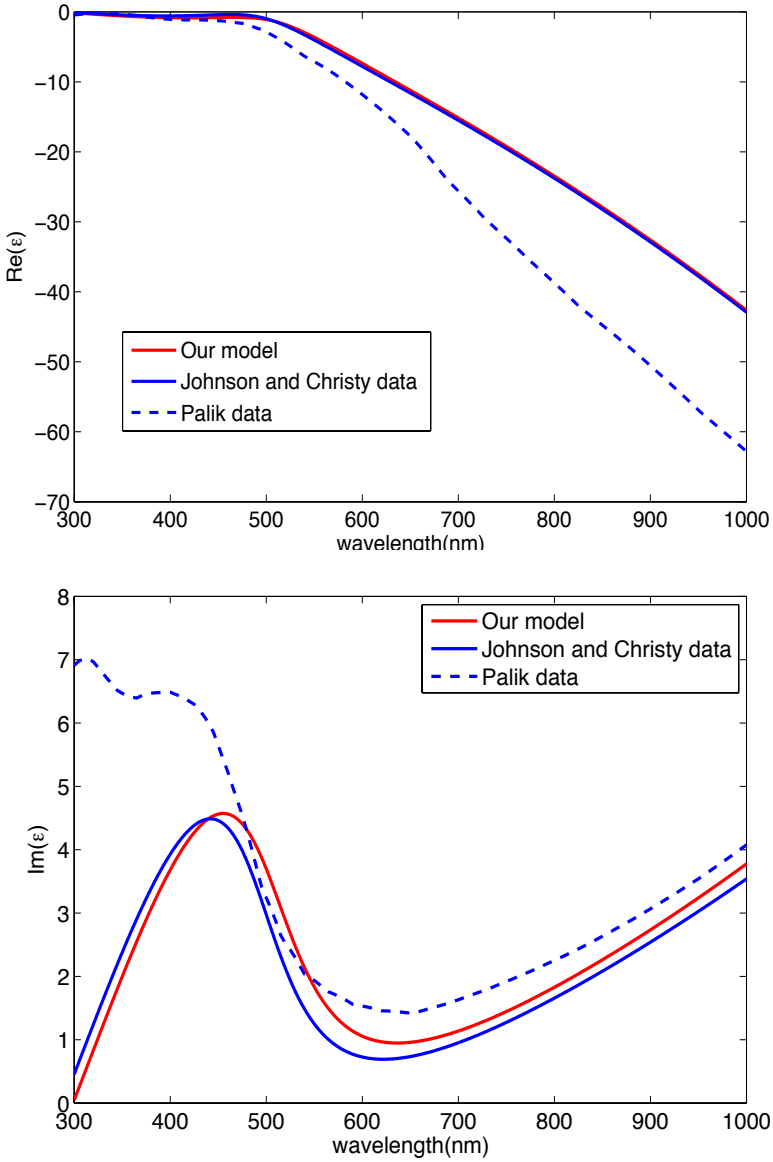

Figure 2.3. Comparison between the real (top figure) and imaginary (bottom figure) part of the permittivity of gold (Au) obtained using the developed model (Red) against the values measured by Palik (Blue dash line) and Johnson and Christy (blue). The fitting was done focusing on the wavelength range from 300 nm - 1000 nm where the most prominent variations in the permittivity of gold occur

2.3 Plasmonic metamaterials (linear properties)

Metamaterials are materials whose optical properties are derived from the structure of the materials composing it. Generally, metamaterials are composed of "meta-atoms" which are individual elements whose structure is repeated through all the metamaterial[13]. In the case of a metamaterial based on nanorods, a meta-atom

corresponds to only one nanorod within a square-base unit cell of size one nanorod period as shown in figure 2.4.

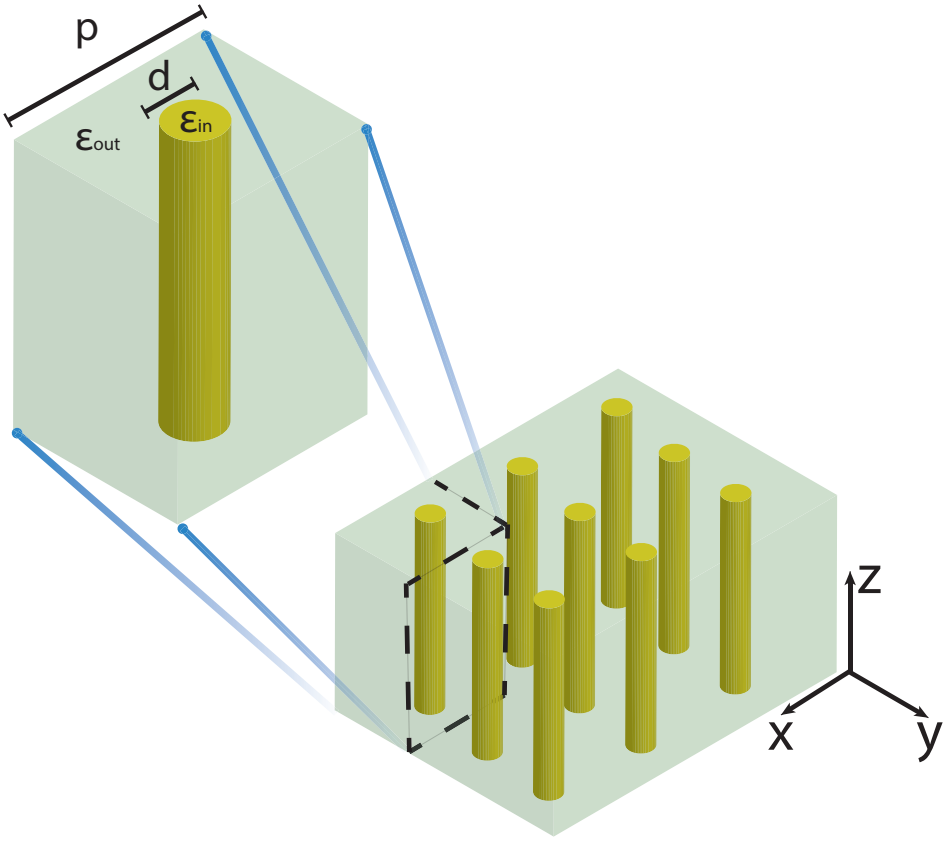

Figure 2.4. Schematic of a nanorod-array based metamaterial showing the permittivity of the embedding medium (ε_{in}) and of the rod (ε_{out}).

The resultant optical properties are a consequence of averaging the optical properties of all the meta-atoms. Given that all the meta-atoms are equal, the average electric field over the whole metamaterial is the average electric field over a single meta-atom:

$$\langle \vec{E} \rangle = \frac{1}{V} \int_V \vec{E} d^3 r \tag{2.21}$$

Where V is the volume of a meta-atom. Therefore an effective permittivity ε_{eff} can be defined between the average electric field and the average displacement field (defined in the same fashion of equation 2.21):

$$\langle \vec{D} \rangle = \varepsilon_{eff} \langle \vec{E} \rangle \tag{2.22}$$

Equation (2.22) is known as an effective medium approximation [13].The meta-atoms of a nanorod based metamaterial (a nanorod unit cell) have anisotropic properties because the structure of the nanorod is isotropic in the x and y direction but varies in the z direction. In this case ε_{eff} is an anisotropic tensor:

$$\varepsilon_{eff} = \begin{bmatrix} \varepsilon_{\perp} & 0 & 0 \\ 0 & \varepsilon_{\perp} & 0 \\ 0 & 0 & \varepsilon_{\parallel} \end{bmatrix} \tag{2.23}$$

Where $\varepsilon_{\perp}$ is the permittivity along the x and y direction and $\varepsilon_{\parallel}$ is the permittivity along the z direction (Figure 2.3). Notice that this approximation assumes an homogeneous electric field over the meta-atom. In the case the field is not homogeneous ε_{eff} will have additional contributions from non-diagonal terms. The value of $\varepsilon_{\perp}$ and $\varepsilon_{\parallel}$ are dependent on the permittivities of the composing materials. Their value can be obtained by calculating the average electric and displacement field of an infinitely large metamaterial along all the directions [14]. Therefore one meta-atom of this material corresponds to an infinitely long rod as seen in figure 2.3. If the rod is placed in a uniform electric field $\vec{E}_{out}$, a polarization field $\vec{E}_{in}$ is created inside it, having the same direction of $\vec{E}_{out}$. Thus the field $\vec{E}_{in}$ must satisfy the boundary conditions at the surface of the rod. If the direction of $\vec{E}_{out}$ is perpendicular to the rod axis (i.e. the x direction or the y direction), the boundary conditions are the continuity of the tangential component of the electric field and of the normal component of the displacement field. Furthermore it can be shown that for the fields given before the corresponding potentials outside and inside the rod in cylindrical coordinates are [15] :

$$\phi_{in} = E_{in} r \cos\phi \tag{2.24}$$

$$\phi_{out} = (E_{out} r - \frac{B_1}{r}) \cos\phi \tag{2.25}$$

where B_1 is a constant found through the boundary conditions which are $-\partial\phi_{in}/\partial\phi\big|_{r=d/2} = -\partial\phi_{out}/\partial\phi\big|_{r=d/2}$ for the tangential electric field components and $-\varepsilon_{in}\,\partial\phi_{in}/\partial r\big|_{r=d/2} = -\varepsilon_{out}\,\partial\phi_{out}/\partial r\big|_{r=d/2}$ for the normal displacement field components (ε_{in} ε_{out} and d are defined as shown in Figure 2.3), generating the following system of equations:

$$\begin{aligned} E_{out} - \frac{4B_1}{d^2} &= E_{in} \\ \varepsilon_{out}(E_{out} + \frac{4B_1}{d^2}) &= \varepsilon_{in}E_{in} \end{aligned} \tag{2.26}$$

Solving equations (2.26) we obtain:

$$\frac{2\varepsilon_{out}}{\varepsilon_{out}+\varepsilon_{in}}\vec{E}_{out} = \vec{E}_{in} \tag{2.27}$$

Since $\vec{E}_{in}$ has the same direction as $\vec{E}_{out}$. Therefore using equation (2.21) the average electric field in the x and y direction is:

$$\left\langle \vec{E}_{\perp} \right\rangle = N\vec{E}_{in} + (1-N)\vec{E}_{out} = N\vec{E}_{in} + (1-N)\frac{\varepsilon_{out}+\varepsilon_{in}}{2\varepsilon_{out}}\vec{E}_{in} \tag{2.28}$$

Where $N = \pi(d/2)^2/p^2$ corresponds to the inclusion fraction which is the ratio between the volumes of the rod and the meta-atom. The same analysis can be done for the displacement field where it is obtained:

$$\left\langle \vec{D}_{\perp} \right\rangle = N\varepsilon_{in}\vec{E}_{in} + (1-N)\varepsilon_{out}\vec{E}_{out} = N\varepsilon_{in}\vec{E}_{in} + (1-N)\frac{\varepsilon_{out}+\varepsilon_{in}}{2}\vec{E}_{in} \tag{2.29}$$

Therefore through equation (2.22), (2.28) and (2.29) it is possible to find the effective permittivity along the x and y direction.

$$\varepsilon_{\perp} = \frac{N\varepsilon_{in}\varepsilon_{out} + (1-N)\varepsilon_{out}\dfrac{\varepsilon_{out}+\varepsilon_{in}}{2}}{N\varepsilon_{out} + (1-N)\dfrac{\varepsilon_{out}+\varepsilon_{in}}{2}} \tag{2.30}$$

If the direction of $\vec{E}_{out}$ is parallel to the rod axis (i.e. the z direction), the only boundary condition that needs to be satisfied is that the tangential components of the electric field are continuous in the rod surface. Therefore $E_{in} = E_{out}$ and the analysis is simpler. The average electric field is then:

$$\left\langle \vec{E}_{\parallel} \right\rangle = N\vec{E}_{in} + (1-N)\vec{E}_{out} = \vec{E}_{in} \tag{2.31}$$

and the average displacement field is:

$$\left\langle \vec{D}_{\parallel} \right\rangle = N\varepsilon_{in}\vec{E}_{in} + (1-N)\varepsilon_{out}\vec{E}_{out} = N\varepsilon_{in}\vec{E}_{in} + (1-N)\varepsilon_{out}\vec{E}_{in} \tag{2.32}$$

Therefore the effective permittivity along the z-direction is:

$$\varepsilon_{\parallel} = N\varepsilon_{in} + (1-N)\varepsilon_{out} \tag{2.33}$$

Experimentally, the nanorods composing the metamaterial may be very small and their optical properties can be approximated better to those of elongated ellipsoids rather than to infinitely long rods. Therefore within this model both $\varepsilon_{\parallel}$ and $\varepsilon_{\perp}$ are dependent on the rod length. The details of this model can be found in [16]. Indeed this model provides better precision quantitatively in the description of the optical response of low aspect ratio nanorods, whereas equations (2.30, 2.33) provide a better description for high aspect ratio nanorods. However both models provide qualitatively the same features and equations (2.30, 2.33) allow an accurate description of the nanorod systems analysed through this entire thesis.

The anisotropic tensor-like permittivity of the nanorods makes their optical properties polarization dependent. Thus for plane waves with electric field $\vec{E} = E_x \exp(i(k_x x + k_y y + k_z z))\hat{i}$ (electric field perpendicular to the nanorods axis or TE polarized) the dispersion relation is [17]:

$$k_x^2 + k_y^2 + k_z^2 = \varepsilon_{\perp} k_0^2 \tag{2.34}$$

Here $k_{x,y,z}$ are the components of the wave vector and $k_0 = 2\pi / \lambda$ is the magnitude of the wave vector in vacuum. These are called ordinary waves since they follow a similar relation to that of waves propagating in an isotropic medium. For plane waves with electric field $\vec{E} = (E_y \hat{j} + E_z \hat{k}) \exp(i(k_x x + k_y y + k_z z))$ (electric field parallel to the nanorod axis or TM polarized) the dispersion relation is:

$$k_x^2 + k_y^2 + \frac{\varepsilon_{\parallel}}{\varepsilon_{\perp}} k_z^2 = \varepsilon_{\parallel} k_0^2 \tag{2.35}$$

These are called extraordinary waves. Unlike equation (2.34) which depends solely on $\varepsilon_{\perp}$, equation (2.35) defines two different regimes depending on the sign of the real part of $\varepsilon_{\parallel}$ and $\varepsilon_{\perp}$. If both have the same sign, equation (2.35) defines an ellipse (elliptic dispersion) with respect to the components of the wave vector ($k_{x,y,z}$) whereas if they have different sign it defines a hyperboloid (hyperbolic dispersion). An elliptic dispersion allows the same optical properties as the spherical dispersion corresponding to isotropic materials, such as a maximum value in the magnitude of the wave vector depending on the refractive index. In contrast a hyperbolic dispersion has no limit in the magnitude of the wave vector. Since the spatial extent of the wave is related to the inverse of the wave vector, the hyperbolic dispersion allows the propagation of highly confined waves [18]

Additionally in the case of extraordinary waves it is possible to define an effective permittivity (ε_{TM}). Therefore we can assume the following dispersion relation at the place of equation (2.35)

$$k_x^2 + k_y^2 + k_z^2 = \varepsilon_{TM} k_0^2 \tag{2.36}$$

For a wave coming from a medium with permittivity ε_0 at an angle of incidence (θ_i), inpinging at the surface of the anisotropic medium, it can be demonstrated using both equations (2.35, 2.36) that ε_{TM} depends on θ_i. Thus replacing k_z^2 in equation (2.35) using equation (2.36), and using Snell's law to obtain $k_x^2 + k_y^2 = k_0^2 \varepsilon_0 \sin^2 \theta_i$, we obtain the following expression for ε_{TM} [16]:

$$\varepsilon_{TM} = \varepsilon_{\perp} + \varepsilon_0 \sin^2 \theta_i (1 - \frac{\varepsilon_{\perp}}{\varepsilon_{\parallel}}) \tag{2.37}$$

In chapter 4 I will recall equations (2.30), (2.33), (2.37) but in that case I will replace the permittivity ε_{in} with that of a metal, allowing the description of our plasmonic metamaterial; a gold nanorod array. I will now discuss the different consequences on the values of the effective permittivity and I will describe the different features of the optical response of this kind of metamaterials.

2.4 Theory for the nonlinear behavior of metals.

The definition of the nonlinear refractive index defined through equation 2.8 is indirectly related to the theory developed in the section 2.2, as the nonlinear refractive index is intensity dependent rather than electron and lattice temperature dependent. Therefore this section is devoted to the analysis of the relation between electron temperature and the intensity of the incident beam. This will allow us to analyze the results obtained through our experimental technique (the z-scan described in the next chapter) with the theory developed in all the previous sections.

Equation (2.8) relates the nonlinear refractive index to the intensity of the beam. This intensity corresponds to the power of the beam, which is the variation of the beam's energy over a period of time. Experimentally since the variation of the refractive index

is measured over a time interval in which a beam of given intensity illuminates the sample, this definition allows a good approximate description of the nonlinear optical response of the material. However theoretically this is not an accurate description of the value of the refractive index. Consider the measurement of the refractive index at a given time t. At that time the value of the refractive index is n(t). If the material is nonlinear, n(t) depends on the value of the beam intensity $I_0(t)$ applied at the time of the measurement of n(t). Thus, since the intensity is defined as $I_0(t) = (E(t) - E(t_0))/(t - t_0)$, it depends on the value of the beam's energy at a certain time t_0 and the value of the energy at time t. Thus n(t) depends on a certain time t_0 and the energy at that time. However the electron and phonon temperature dependence of the metallic permittivity described in section 2.2, implies that n(t) only depends on the energy of the electrons and phonons at a given time t and it is not relative to any specific time t_0.

To overcome this problem, it is possible to define a nonlinear refractive index n(t) depending on the energy stored in the material at time t ($E_s(t)$). This stored energy corresponds to the additional energy within the material causing the modification of the material's optical properties. Therefore the stored energy is modified as the material absorbs additional energy provided by an input energy from an incoming beam $E_i(t)$. Thus the stored energy at a time t+dt is related to the stored energy at time t through:

$$E_s(t + dt) = AdE_i + E_s(t) \tag{2.38}$$

Where A is the material's absorption and dE_i is the input energy provided in a time dt. Since the absorption of the material is dependent on its refractive index, thus A depends

on the stored energy. Dividing equation (2.34) by dt and showing explicitly the dependence of A on the stored energy, we obtained:

$$\frac{dE_s(t)}{dt} = A(E_s(t))I_i(t) \tag{2.39}$$

where $I_i(t) = dE_i(t)/dt$ is the input intensity. Equation (2.39) defines then the evolution of the stored energy in the material for a given input beam intensity. This equation can be easily solved if A is expanded using taylor to first order with respect to $E_s(t)$.

Therefore equation (2.39) becomes

$$\frac{dE_s(t)}{dt} = (A_0 + \left.\frac{dA}{dE_s}\right|_{E_s=0} E_s(t))I_i(t) \tag{2.40}$$

The solution is:

$$E_s(t) = \frac{A_0}{B_0}(\exp(B_0 \int_0^t I_i(t')dt') - 1) \tag{2.41}$$

where $B_0 = dA/dE_s|_{E_s=0}$. The dependence in the linear absorption on the stored energy implied by equation (2.41) shows that the nonlinear properties depend on the linear properties of the medium. This is an important remark since I will show in Chapters 4 and 6 that through the design of the linear properties the nonlinear properties can be enhanced strongly.

In the experiments the input intensity is provided through femtosecond pulses. Thus assuming that these pulses have a Gaussian profile in time, the intensity of these pulses is $I(t) = I_0 \exp(-t^2/2t_d{}^2)$ where t_d is the pulse duration and I_0 is the maximum intensity of the pulse. This intensity is related to the total pulse energy (E_p) through $I_0 = E_p/(t_d\sqrt{\pi})$. Furthermore using equation (2.41) the stored energy is $E_s = (A_0/B_0)(\exp(B_0E_p) - 1)$. Thus we can compute the variation of the material's

refractive index and this one must be equivalent to the variation obtained using equation (2.8). Therefore:

$$n(E_s) - n_0 = n_2 I_0 \tag{2.42}$$

and n_2 (both real and imaginary parts) can be calculated to compare the results obtained experimentally and theoretically. In the particular case of metals, the stored energy is directly related to the energy of the electron gas in the conduction band:

$$E_s = (1/2) C_e T_e^{\,2} V \tag{2.43}$$

Where V is the volume of the material storing energy. Therefore the theory used in section 2.2 (and section 2.3 as it will be shown in chapter 4) can be used together with equations (2.41-2.43) to calculate the theoretical value of n_2 for a metal.

As a final remark it is worth mentioning that in equation (2.39) there is no mechanism added leading to the decrease of the stored energy by the material. In the case of metals there is a mechanism related to the electron-phonon scattering. However since the nonlinear properties are being measured using femtoseconds pulses (as it will be shown in the next chapter), during this short period of time, the contribution of this scattering is very small and can be neglected.

2.5 Conclusion

In this chapter I have given the basic theory that allows us to understand and characterize the linear and nonlinear optical properties of metals showing how the intensity of light increases the scattering of the electrons in the conduction band modifying their optical response. The ultrafast dynamics of this process renders this nonlinear behaviour attractive for applications in ultrafast nonlinear optics. Additionally I have given an introduction to the effective medium theory, which is used to describe

the linear optical properties of a nanorod array obtaining an effective permittivity dependent on the materials composing them and the dimensions of the nanorods. Finally I have shown how the variation of the refractive index of a nonlinear material is directly related to the energy stored in it, which in our case is provided optically. In chapter 4, I will show through these equations that the high optical nonlinearity of a gold nanorod array around the plasmon resonances is related to their high optical absorption.

References

[1] R. W. Boyd, *Nonlinear optics*, 3rd ed. Amsterdam ; Boston: Academic Press, 2008.

[2] R. Loudon, *The quantum theory of light*, 3rd ed. Oxford ; New York: Oxford University Press, 2000.

[3] P. H. Bucksbaum, "Attophysics: Ultrafast control," *Nature,* vol. 421, pp. 593-594, 2003.

[4] D. E. Spence, P. N. Kean, and W. Sibbett, "60-fsec pulse generation from a self-mode-locked Ti:sapphire laser," *Optics Letters,* vol. 16, pp. 42-44, 1991.

[5] R. W. Boyd, *Nonlinear optics*, 3rd ed. Amsterdam ; Boston: Academic Press, 2008, Page 5.

[6] D. Pines, *Elementary excitations in solids*. New York,: W.A. Benjamin, 1963.

[7] J. Y. Bigot, J. Y. Merle, O. Cregut, and A. Daunois, "Electron Dynamics in Copper Metallic Nanoparticles Probed with Femtosecond Optical Pulses," *Physical Review Letters,* vol. 75, pp. 4702-4705, 1995.

[8] D. Pines and P. Nozières, *The Theory of Quantum Liquids: Normal Fermi liquids*: W.A. Benjamin, 1966.

[9] R. T. Beach and R. W. Christy, "Electron-electron scattering in the intraband optical conductivity of Cu, Ag, and Au," *Physical Review B,* vol. 16, pp. 5277-5284, 1977.

[10] J. Hohlfeld, S. S. Wellershoff, J. Güdde, U. Conrad, V. Jähnke, and E. Matthias, "Electron and lattice dynamics following optical excitation of metals," *Chemical Physics,* vol. 251, pp. 237-258, 2000.

[11] P. B. Johnson and R. W. Christy, "Optical Constants of the Noble Metals," *Physical Review B,* vol. 6, pp. 4370-4379, 1972.

[12] E. D. Palik, *Handbook of Optical Constants of Solids*: Academic Press, 1998.

[13] W. Cai and V. Shalaev, *Optical Metamaterials: Fundamentals and Applications*: Springer, 2009.

[14] J. Elser, R. Wangberg, V. A. Podolskiy, and E. E. Narimanov, "Nanowire metamaterials with extreme optical anisotropy," *Applied Physics Letters,* vol. 89, pp. -, 2006.

[15] J. D. Jackson, *Classical electrodynamics*: Wiley, 1975. Pages 77, 157

[16] R. Atkinson, W. R. Hendren, G. A. Wurtz, W. Dickson, A. V. Zayats, P. Evans, *et al*., "Anisotropic optical properties of arrays of gold nanorods embedded in alumina," *Physical Review B,* vol. 73, p. 235402, 2006.

[17] J. J. A. Fleck and M. D. Feit, "Beam propagation in uniaxial anisotropic media," *Journal of the Optical Society of America,* vol. 73, pp. 920-926, 1983.

[18] A. Poddubny, I. Iorsh, P. Belov, and Y. Kivshar, "Hyperbolic metamaterials," *Nature Photonics,* vol. 7, pp. 948-957, 2013.

Chapter 3: Z-scan technique

In this chapter the Z-Scan technique, the experimental method used to measure the intensity dependent refractive index will be described. Firstly the experimental curves obtained through this technique; the close aperture curve and open aperture curve will be described theoretically. It will be shown that these curves can be easily represented as a simple polynomial function dependent on the real and imaginary part of the third order nonlinear susceptibility. Secondly I will describe the setup built for the realization of the Z-scan technique. This setup will be composed of different optical elements allowing the polarization, wavelength and angle dependence of the measurements. Finally, as an example of the measurements obtained through the z-scan technique, I will characterize the third order nonlinear susceptibility of gold smooth film at wavelengths close to the interband transition (~550 nm). The results obtained will be compared to those predicted through the theory presented in chapter 2.

3.1 The Z-Scan technique.

To characterize the optical properties of any material, its optical reflection (the ratio between the incident intensity and the reflected intensity) and transmission (the ratio between the incident intensity and the transmitted intensity) is usually measured. These two are linked directly to the refractive index of the material and therefore through them it is possible to derive its value. The same analysis applies for a material with an intensity dependent refractive index (I will refer to these materials as nonlinear materials). However as a consequence of equation (2.8), the measured value of the refractive index depends on the intensity of light used in the measurement. Therefore it is possible to conclude that several measurements at different intensities are needed to retrieve the value of the corresponding nonlinearity of the nonlinear material related to n_2.

In 1990 in a paper called "Sensitive measurement of optical nonlinearities using a single beam" a method was proposed to allow the measurement through a continuum range of intensity values, of the optical transmissibility through a given nonlinear material[1].

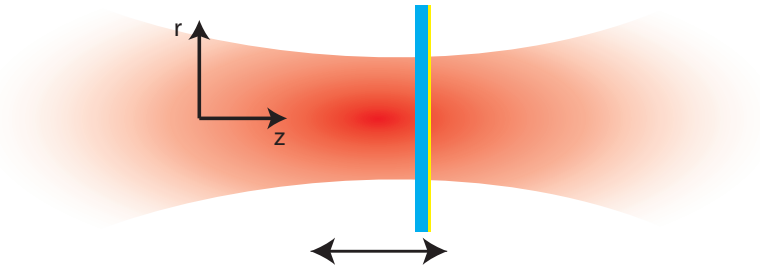

Figure 3.1 Thin film of a nonlinear material (yellow film) scanned through the focus of a Gaussian beam.

This is achieved by scanning a thin film of the nonlinear material over different position values around the focus of a Gaussian beam as shown in figure 3.1.

Assuming a TEM_{00} Gaussian beam of beam waist radius w_0 travelling in the z+ direction and having its focus at $z = 0$, its intensity is:

$$I(r,z) = I_0\left(\frac{w_0}{w(z)}\right)^2 \exp(-\frac{2r^2}{w^2(z)}) \tag{3.1}$$

where $w^2(z) = {w_0}^2(1 + z^2 / z_0^2)$ is the beam radius with $z_0 = k{w_0}^2 / 2$ is the diffraction length of the beam and $k = 2\pi / \lambda$ is the relation between the wave vector and the wavelength. Therefore as a consequence of the intensity dependent refractive index (equation (2.8)) and equation (3.1), the optical field transmitted through the thin film varies according to the position of the film on the Gaussian beam. Furthermore if the film is thin such that $L < z_0$, the value of the refractive index at a certain position over the film depends solely on the intensity value at that point ($I(r,z)$) and the contributions from self-refraction processes occurring as a result of the propagation of the Gaussian beam through the nonlinear material, will be negligible. [1]. Under this condition through this method known as "*Z-Scan*", the nonlinear processes occurring in the nonlinear thin film can be characterized by measuring two of the nonlinear effects affecting the transmitted optical field: self-focusing and nonlinear absorption.

Self-focusing is a consequence of the phase added to the wave as a result of the field's propagation through the nonlinear material. This phase can be expressed in terms of the intensity dependent refractive index and the effective length of the thin film ($L_{eff} = (1 - e^{-\alpha L}) / \alpha$ with L being the film thickness and α is the linear absorption). Using equation (2.8) we obtain:

$$\phi = k(n_{0r} + n_{2r}I)L_{eff} = k(n_{0r})L_{eff} + k(n_{2r}I)L_{eff} = \phi_l + \phi_{nl} \tag{3.2}$$

Where the sub index r corresponds to the real part of n_0 and n_2. Therefore the first term is the linear phase (ϕ_l), which does not depend on the intensity whereas the second phase is the nonlinear phase (ϕ_{nl}) dependent on the intensity. Using equation (3.1) we find that the nonlinear phase is dependent on both r and z:

$$\phi_{nl} = k(n_{2r}I)L_{eff} = k(n_{2r}I_0)(L_{eff}\left(\frac{w_0}{w(z)}\right)^2 \exp(-\frac{2r^2}{w^2(z)})) \tag{3.3}$$

Equation (3.3) is written suggestively to show that the added nonlinear phase can also be thought of the phase added by the propagation through a film having refractive index ($n_{2r}I_0$) but with a Gaussian varying thickness. Therefore taking into account both linear and nonlinear phases, the propagation through the nonlinear thin film is similar to the propagation through a divergent or convergent lens depending on whether the value of n_{2r} is negative or positive as shown pictorically in figure 3.2.

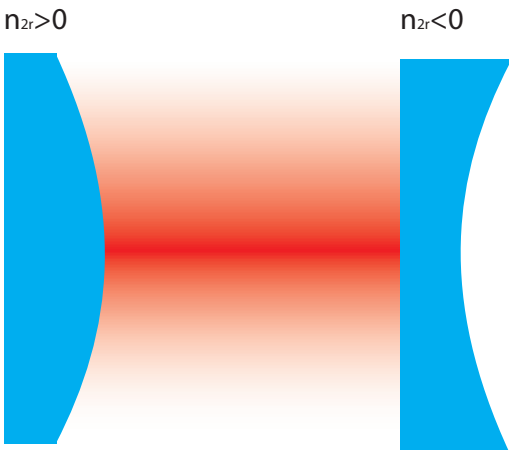

Figure 3.2 Gaussian shaped divergent and convergent lens corresponding to the two possible signs of the nonlinear refraction. The beam profile is shown (red) to evidenced the modification of the effective film thickness in each case

Thus the transmitted optical field will experience focusing or defocusing depending on the sign of n_{2r}.

The detection of this optical effect can be achieved by measuring the variation in the transmitted optical intensity of the optical field through an aperture positioned after the thin film against the position of the film (z) as shown schematically in figure 3.3(a).

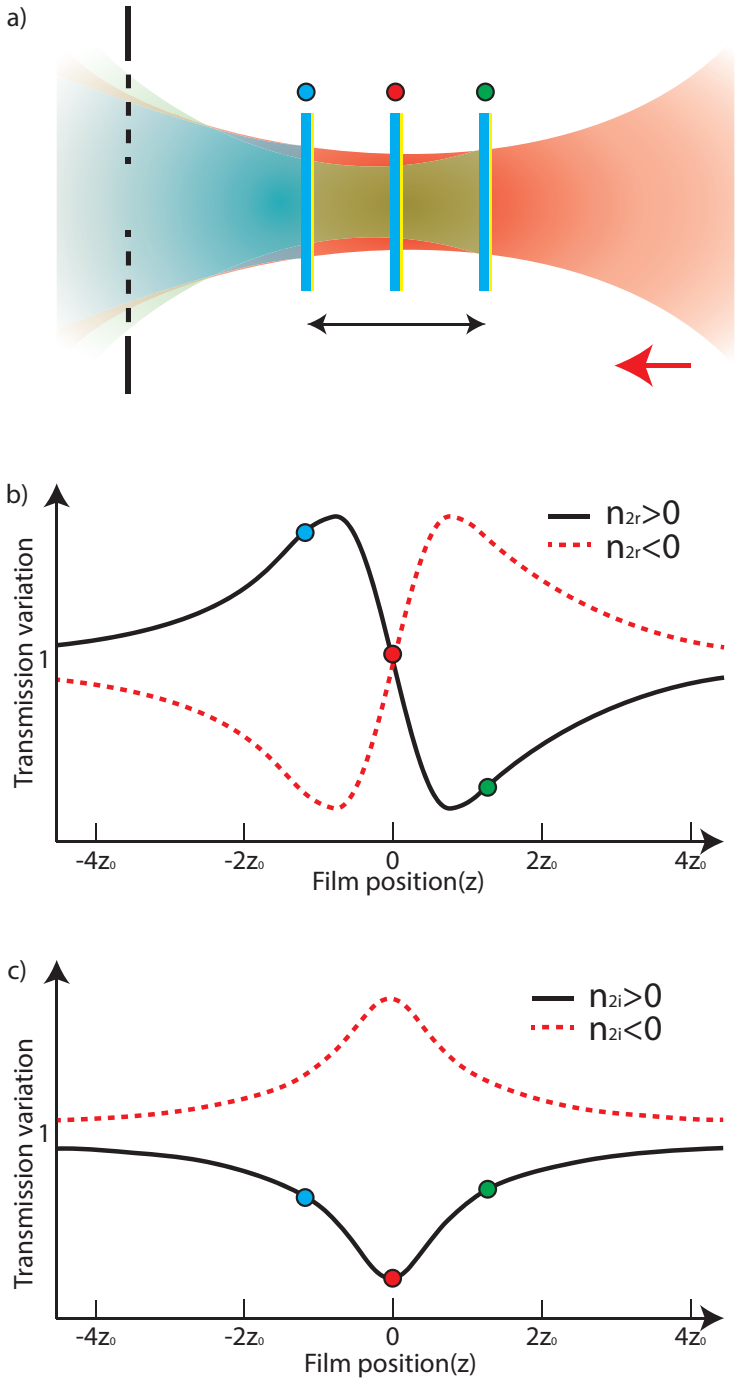

Figure 3.3. The dots indicate the position of the sample (blue) before the focus (red) at the focus (green) after the focus of the Gaussian beam a) Schematic of the z-scan having at the output an aperture with variable size represented by the dashed line in the left. The colored beams in the left represent the self-focusing obtained at every position marked by the dots. The color of the beam is related to the color of the dot. The red arrow represents the direction of propagation of the beam b) Typical close aperture curves. c) Typical open aperture curves. Both positive (black) and negative (red dashed line) cases are shown. The curves in b) and c) were plotted using equations (3.6) and (3.8)

Indeed, in the case of a positive sign of n_{2r}, when the film is positioned outside but before the focus of the Gaussian beam, the focus of the transmitted optical field is shifted towards the film. Thus, the optical field reaching the aperture is more spread out and the transmitted intensity after the aperture is reduced. After the focus, the film focuses the transmitted optical field, increasing the transmitted intensity after the aperture. The inverse effect occurs for the negative sign of n_{2r}. The variation of the transmission after the aperture is $T_{nl}(z)/T_0$ with $T_{nl}(z)$ being the total transmission after the aperture and T_0 being the linear transmission measured either at low intensity or away from the Gaussian beam focus in order to obtained a negligible dependence on the beam intensity. The curves obtained when plotting the variation of the transmission against the sample position (z) are shown for both cases in figure 3.3(b). The mathematical expression for these curves can be obtained by expanding the transmitted beam as a series of Gaussian beams with different diffraction. In the far field (the aperture position is far from the thin film at a distance $d >> z_0$) and for a small size aperture having a transmission $S << 1$ it can be shown [1, 2] that the resultant expression can be approximated as:

$$\frac{T_{nl}(z)}{T_0} \simeq 1 + \frac{4\Delta\phi_0 x}{(x^2+9)(x^2+1)} \tag{3.4}$$

With $\Delta\phi_0 = kn_{2r}I_0L_{eff}$, $x = z/z_0$ and the scanning direction is from negative to positive values of z. The use of this expression for the fitting analysis of the measured curves will be shown later in this chapter. In conclusion, by scanning the film along the focus of a Gaussian beam it is possible to measure its self-focusing through the measurement of the transmission variation after an aperture. Thus, without the aperture, all the

transmitted intensity will be measured and the effect of the self-focusing will not be observed in the z-scan.

Nonlinear absorption is the dependence of the film absorption to the intensity of the beam. Thus the transmitted intensity is computed through the intensity dependent absorption coefficient $\alpha'(I)$ through:

$$I = I_0 \exp(-\alpha'(I)L_{eff}) = I_0 \exp(-(\alpha + \beta I)L_{eff}) \tag{3.5}$$

With α being the linear absorption coefficient and β being the nonlinear absorption coefficient. Thus depending on the incident intensity on the film, the transmitted intensity will be either reduced or increased depending on the sign of β. In the same fashion as equation (3.3), we obtained through equation (3.1) a position dependent absorption:

$$\beta I(r,z)L_{eff} = \beta I_0 L_{eff} \left(\frac{w_0}{w(z)} \right)^2 \exp(-\frac{2r^2}{w^2(z)}) \tag{3.6}$$

Therefore the maximum variation in the absorption is obtained when the film is at the focus of the Gaussian beam, whereas away from the focus this variation decreases. The measurement of this variation can also be realized by measuring the transmission variation after the film ($T_{nl}(z)/T_0$) directly obtaining the curves shown in figure 3.3c. Notice that in this case there will be a transmission variation regardless of the aperture size as this variation is a direct consequence of the film's nonlinear absorption. Furthermore, it can be shown that in the far field the transmission variation can be approximated as:

$$\frac{T_{nl}(z)}{T_0} \simeq 1 - \frac{2(x^2+3)\Delta\psi}{(x^2+9)(x^2+1)} \tag{3.7}$$

With $\Delta\psi = \beta I_0 L_{eff}/2$. The imaginary part of n_2 is related to the nonlinear absorption coefficient using $\beta = 2kn_{2i}$ and through this measurement its value is obtained.

In general a material can have both real and imaginary part of n_2, thus the measurement of the transmission variation after the aperture (with transmission S<<1) has the contribution of both self-focusing and nonlinear absorption. Therefore the expression of the transmission variation is a combination of equations (3.4) and (3.7):

$$\frac{T_{nl}(z)}{T_0} \simeq 1 - \frac{2(x^2+3)\Delta\psi}{(x^2+9)(x^2+1)} + \frac{4\Delta\phi_0 x}{(x^2+9)(x^2+1)} \tag{3.8}$$

In order to distinguish between both of them an additional measurement without the aperture is necessary. This measurement will be only sensitive to the nonlinear absorption and the curve obtained can be readily fitted using only equation (3.7) obtaining the value of $\Delta\psi$. Afterwards using this value and equation (3.8), the measurement of the transmission variation after the aperture can be fitted obtaining $\Delta\phi_0$. The measurement without the aperture is known as *open aperture z-scan*, whereas the measurement with the aperture is known as *close aperture z-scan*.

In the following section, I will describe the experimental setup used to perform the z-scan. Additionally in section 3.3 I will describe the measurement of the real and imaginary part of n_2 for gold around 550 nm where I will emphasize in the fitting analysis used in combination with equations (3.7) and (3.8) to find with an specific error in the values of $\Delta\phi_0$ and $\Delta\psi$.

3.2 The z-scan setup

The diagram containing all the elements required to perform a z-scan measurement is shown in figure 3.4. The diagram is divided in three different sections: The femtosecond laser, the z-scan setup and the compression setup.

The femtosecond laser generates light pulses, which are used for the z-scan measurement. The laser is based on a Ti:Saphire crystal which is pumped through a 532 nm wavelength beam to generate 800 nm wavelength pulses at a repetition rate of 150 kHz having a pulse duration of 50 fs. These pulses are sent to an optical parametric amplifier (OPA), which through wave mixing processes generates at the output p-polarized pulses having a broad wavelength range between 550 nm and 1700 nm.

At the input of the z-scan setup, a half-wave plate (λ/2) to change as desired the polarization of the beam, for polarization dependent z-scan measurements. Additionally there is an optical density (OD) to control the input power into the z-scan, to control the nonlinear response of the sample being analyzed. Subsequently the light is divided through a glass slide into a path going towards a detector (D1) and a path going towards a beam expander (BE). The beam expander increases the radius of the beam to fill the input of an objective.

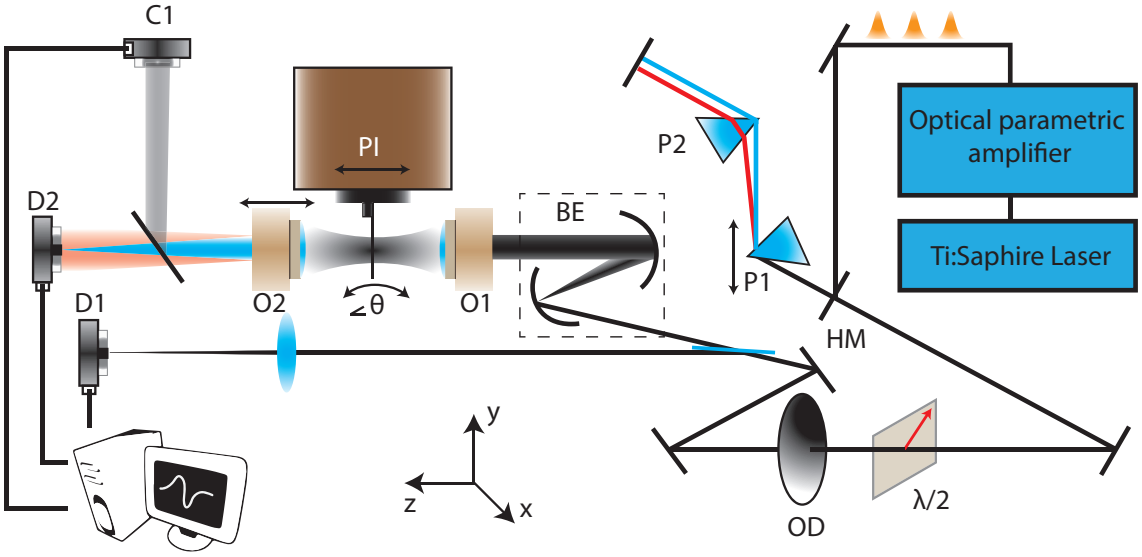

Figure 3.4 Schematic z-scan. (HM) Half-mirror; the beam is reflected and then in the return path it is transmitted above the mirror. (λ /2) Half-wave plate. (OD) optical density. (BE) Beam expander (O1, O2) Objectives. (P1,P2) Prisms. (D1, D2) Photodiode detectors. (C1) CCD camera. (PI) Piezo positioner (θ) The sample can be tilted as shown with the arrows for angular dependent measurements.

Therefore the light will be focused to a diffraction-limited spot to achieve the maximum intensity illuminating the sample and the beam waist at the focus will be related to the numerical aperture (NA) of the lens through $w_0 = \lambda / (\pi NA)$. The chosen objectives are long working distance objectives, as the sample must rotate for angular dependent measurements.

Furthermore the numerical aperture must be large but not large enough as to make the beam strongly divergent at the output making it difficult to collect all the transmitted power later as required for an open aperture z-scan measurement. Additionally the nanopositioner (PI) scanning range is $z_{range} = 100\ \mu$m and to ensure the z-scan curve is within it, this range must not be smaller than $8z_0$ as can be seen on figure 3.3 (b-c). Therefore there is a limit in the minimum numerical aperture required to do z-scan at a given maximum wavelength. This is

$$z_{range} < 8z_0 = \frac{8\lambda}{\pi NA^2}$$
$$NA > \sqrt{\frac{8\lambda}{\pi z_{range}}} \tag{3.9}$$

Which for a maximum wavelength of 1700 nm this limit is NA > 0.13. In the constructed setup the focusing objective (O1) has a numerical aperture of 0.28 and a focal length of 20 mm whereas the collection objective (O2) has a numerical aperture of 0.42 and a focal length of 10 mm, thus the z-scan curves obtained are well within the translation range of the piezo. After the collection objective a glass slide divides the light into two paths: one towards a detector (D2) and the other towards a CCD camera (C1). The functionality of the CCD camera is to allow the visualization of the beam's position in the sample giving us feedback on whether the beam is positioned in the spot of our interest or on the irregularities on the sample's surface. Additionally it let us

verify if the sample is positioned in the focus of the Gaussian beam, as the sample will be scanned around that point.

The detectors D1 and D2 are InGaAs high-speed photodiodes with a wavelength detection range of 500 nm -1700 nm, rise time of 5 ns and a junction capacitance of 50 pf. The high-speed photodiodes are required in order to collect the electrical signal generated by each pulse. Therefore to compute the transmission of the sample the ratio between the voltages of the detectors is computed allowing a measurement with a low dependence in the fluctuations of the laser intensity. In order to compute this ratio accurately, the electrical signals generated by the same pulse must be compared. In order to ensure this, the detectors are connected to a simultaneous sampling system operating at a speed of 2 MS/s (megasamples per second), which records the voltage signal of the pulses with high time resolution. Additionally, these photodiodes are loaded with a resistance of 50 kΩ producing an RC decay time in the photodiode of $\tau = RC = 2.5\mu s$. The selection of this resistance was done experimentally to allow an increased response in the photodiodes while also having a differentiation between the electrical signals of each pulse according to the separation time between them (the inverse of the repetition rate frequency which is ~6.7 μs). The electrical signals in the photodiodes are recorded using the computer through software built using MATLAB. The electrical signal on both D1 and D2 are integrated over an interval of 1s to average between a large number of pulses. Then the ratio between them is computed obtaining an error of ~0.1% in the measured transmission. The transmission is computed as the sample is scanned over the whole range of the nanopositioner (100 μm) every 1 μm (or less if an increased resolution is needed) obtaining the z-scan curve.

The z-scan can be change between open or close aperture z-scan by moving the collection objective O2. As shown in figure 3.4, depending on the position of O2 the output beam can be collimated, divergent or focused. Thus we can focus the beam onto the detector D2 allowing all the transmitted light to be detected thus realizing an open aperture z-scan (blue beam) or we can diverge it to allow only a part of the beam to be detected to realize a close aperture z-scan (red beam)

The compression setup allows the compensation for the pulse dispersion when this propagates through the objective O1. This is a consequence of the wavelength dependence of the glass refractive index, which is larger for shorter wavelengths. Therefore the phase added to the shorter wavelength components of a pulse is larger thus increasing the pulse duration. The compression setup shown in figure 3.4 is realized with the prisms P1 and P2 to increase the phase added to longer wavelengths through the extra distance they have to travel on the second prism, evidenced by the red line in figure 3.4 (The blue line show the path of the shorter wavelengths). This compression setup can be accessed through the reflection of the beam from a half-mirror (HM). The larger deflection of the blue line with respect to the red line is a consequence of the larger refractive index at shorter wavelengths. As a result at the output of the objective the paths travelled by both longer and shorter wavelengths are the same and the pulse retains its initial duration. Furthermore in order to minimize the reflections of p-polarized light in the compression setup, the angle of incidence of the beam on the prisms must be at the Brewster angle. However this angle varies with wavelength and the compression setup must change according to this variation. Therefore the mirror HM, can be tilted to obtain the angle of incidence required and to

achieve the incidence at the tip of the prism, the input prism (P1) can be moved in the y direction (as shown in figure 3.4).

The distance required between the prism apexes to compensate for the objective O1 dispersion, is found using FROG (Frequency resolved optical gating), which allows the characterization of the pulse in time and wavelength. Therefore we can calibrate this distance in order to obtain the shortest pulse at the output of the objective O1. Once this distance is characterized it is possible to calibrate it even more accurately by slightly changing it while doing a z-scan measurement. Therefore the increased variation of the transmission measured through the z-scan at a given apex distance, will be a signature that the pulse incident on the sample has the shortest duration.

3.3 Z-scan measurements on gold smooth film

From now on for the results shown here and in chapter 4, we shall refer to the real part of the nonlinear refractive coefficient (n_{2r}) as γ, as it is commonly found in the literature [1]. Using the z-scan technique a 50 nm gold film was measured at the wavelengths of 550 nm, 565 nm, 575 nm and 600 nm, which are the wavelengths provided through manual calibration of the OPA.

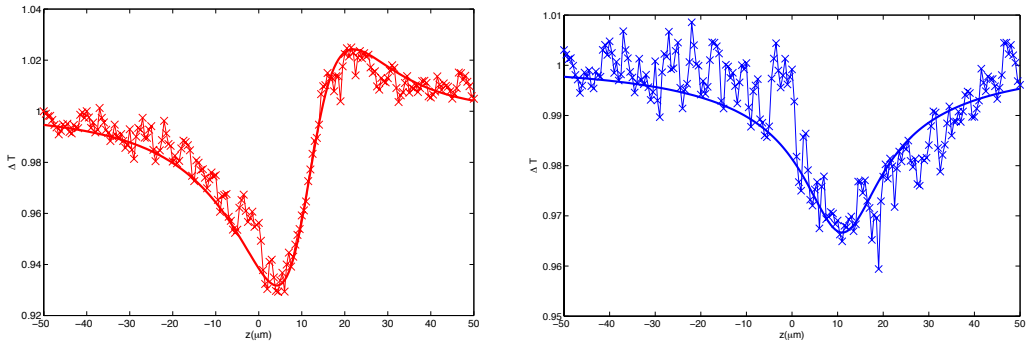

Figure 3.5 (left) Close aperture z-scan on a smooth gold film (50 nm) at a 550 nm wavelength. (right) Open aperture z-scan. Notice the asymmetry of the valley and peak of the close aperture z-scan corresponding to the contributions of both nonlinear absorption and refraction. These curves correspond to $\Delta\phi_0 = 0.2 \quad \Delta\psi = 0.05$

The typical close and open aperture curves corresponding for the case of 550 nm are shown in figure 3.5. Notice that these curves are already fitted using Equation (3.8). This fitting is realized by using the least squares method.

Thus for an obtained transmission variation ΔT from a close aperture or open aperture z-scan, the error between these two curves is calculated through:

$$E = \int (\Delta T^2 - \left(\frac{T_{nl}(z)}{T_0} \right)^2) dz \tag{3.9}$$

Thus E is numerically evaluated for a broad range of values for $\Delta\phi_0$ and $\Delta\psi$ using MATLAB in order to find those values giving the minimum value for E.

Through this method this allows us to obtain the values of $\Delta\phi_0$ and $\Delta\psi$ within an error of ±0.025. Recalling the relations derived in section 3.1 which relate these coefficients to the real and imaginary part of n_2 :

$$\Delta\phi_0 = k\gamma I_0 L_{eff} \qquad \Delta\psi = \beta I_0 L_{eff} / 2 \qquad \beta = 2kn_{2i} \tag{3.10}$$

The values obtained are shown in Table 3.1 The pulse energy is derived, measuring the power of the beam at the input of the z-scan and dividing it by the repetition rate. The value of I_0 corresponding to the beam intensity at the material's surface can be calculated from the pulse energy. Furthermore this value must be normalized to the area of excitation, which corresponds to the area of the Gaussian beam at the focus.

$\lambda(nm)$	$\Delta\psi$	$\Delta\phi_0$	Pulse Energy(nJ)	β (cm/GW)	γ (cm^2/W)
550	0.05	0.2	1	272.32±136	(4.77±0.6)×10^{-12}
565	0.05	0.2	1.33	225.1±112	(4.05±0.5)×10^{-12}
575	0.05	0.2	2.5	127.43±63.7	(2.33±0.3)×10^{-12}
600	0.05	0.1	3	121.7±60.9	(1.16±0.3)×10^{-12}

Table 3.1 β (Nonlinear absorption) and γ (nonlinear refraction) for a gold thin film of 50 nm at different wavelengths. The pulse width is 50 fs.

This can be calculated from the Gaussian beam width, which is related to the numerical aperture. Therefore the normalized intensity is $I_0 = I_0^* / (\pi(aw_0)^2) = I_0^* / (\pi(a\lambda / 2NA)^2)$ where I_0^* corresponds to the total intensity calculated using the pulse energy $I_0^* = E_p / (t_d\sqrt{\pi})$. An additional constant (a) multiplies the value of the waist since according to the resulting z-scan, the theoretical value of the Rayleigh length does not correspond exactly to the value required to fit the obtained z-scan curve, this probably is a consequence of the beam not being a perfect Gaussian beam at the focus. Through the fitting software this constant can be obtained and it is approximately ~ 1.73. The effective length is calculated taking into account the wavelength dependent absorption of the gold film (α) through $L_{eff} = (1 - e^{-\alpha L}) / \alpha$ where L=50 nm. Figure 3.6(a-b) shows a wavelength dependent graph for the values retrieved of γ and β. The values obtained are compared with previous values measured for gold by previous authors [3]. Since the optical nonlinearity of gold depends on the pulse width, only those results obtained having the same pulse widths are compared. An author obtained a result of $n_{2i} = 5.73 \times 10^{-15} m^2 / W$ at 600nm for a pulse width of 200 fs. In our case this result is $n_{2i} = 5.81 \times 10^{-17} m^2 / W$ which is two orders of magnitude smaller. This is in agreement with the statement given by the same author, which says that the optical nonlinearity decreases with the pulse width. This statement is also a consequence of the relation $I_0 = E_p / (t_d\sqrt{\pi})$, which shows how the intensity increases with the pulse width thus making smaller the measured optical nonlinearity. These values are compared using the theory developed in section 2.3. In this case the volume storing energy corresponds to that illuminated by the Gaussian beam at the focus. Thus this volume is $V = \pi(a\lambda / 2NA)^2 L$.

Therefore the evolution of the absorption of that volume is computed over time to calculate the stored energy and then the variation of the refractive index (equations (2.41-2.43)) is compared with the values experimentally obtained. The results are shown in 3.6 (c-d) for both γ and β. Additionally in figure 3.6 (a-b) the red dash line represents the results obtained theoretically for comparision with the experimental results.

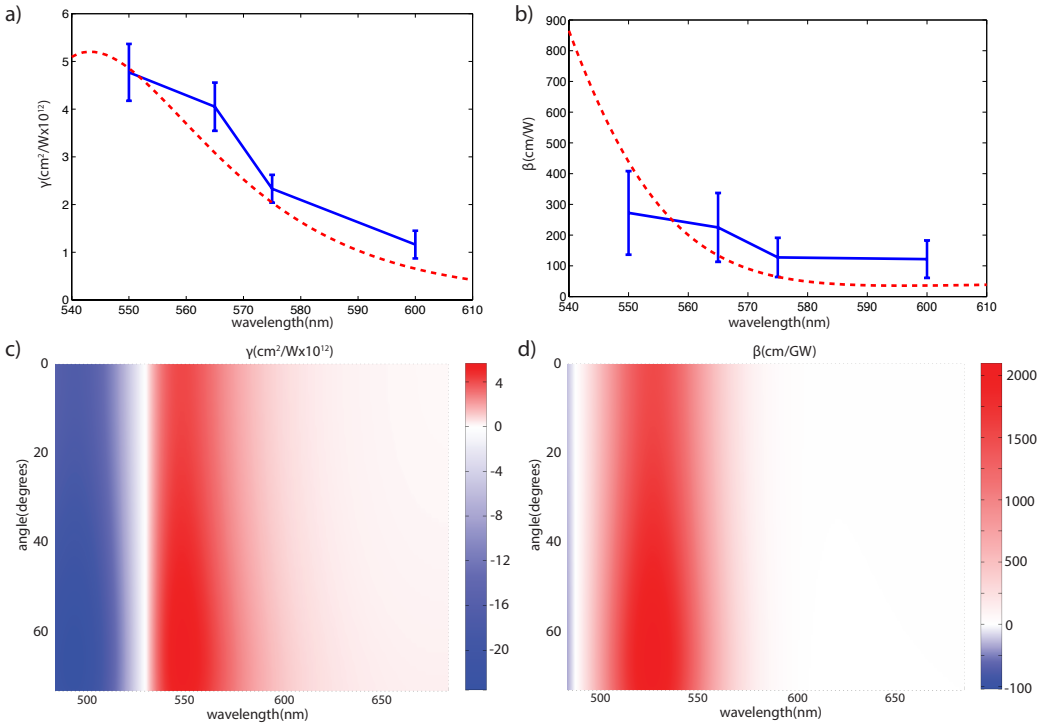

Figure 3.6. Measured (a) nonlinear refraction (b) nonlinear absorption for a L=50 nm gold film on SiO_2. (c-d) Numerically calculated using equation 2.38 against angle of incidence from air. In the numerical calculations a Gaussian shaped 50 fs pulse is assumed. In figure a and b the red dash line is a cross-section from figures c and d at 0 angle of incidence for further comparison with the obtained theoretical values.

As expected the largest value for the optical nonlinearity is obtained around the interband transition of gold (~532 nm). For increasing wavelength both γ and β decrease monotonically.

3.4 Conclusion

The z-scan technique measures both the nonlinear absorption and nonlinear refraction of a thin film by scanning it through the focus of a Gaussian beam. The measured curves can be fitted through polynomial curves obtaining the values of the nonlinear coefficients. Through this technique I have measured the nonlinear optical properties of a gold film at several wavelengths and through the theory developed in chapter two I have shown a good fit to the results obtained experimentally and those obtained theoretically.

References

[1] M. Sheik-Bahae, A. A. Said, T. H. Wei, D. J. Hagan, and E. W. Van Stryland, "Sensitive measurement of optical nonlinearities using a single beam," *Quantum Electronics, IEEE Journal of,* vol. 26, pp. 760-769, 1990.

[2] X. Liu, S. Guo, H. Wang, and L. Hou, "Theoretical study on the closed-aperture Z-scan curves in the materials with nonlinear refraction and strong nonlinear absorption," *Optics Communications,* vol. 197, pp. 431-437, 2001.

[3] R. W. Boyd, Z. Shi, and I. De Leon, "The third-order nonlinear optical susceptibility of gold," *Optics Communications,* vol. 326, pp. 74-79, 2014.

Chapter 4: Experimental characterization and analysis of the linear and nonlinear optical properties of a plasmonic metamaterial

The linear and nonlinear optical properties of a plasmonic metamaterial based on gold nanorod arrays will be characterized in this chapter. Firstly, I will start with the description of the linear optical properties both experimentally and theoretically. It will be shown that our nanorod sample possesses two plasmonic resonances: A transverse resonance at 550 nm and a longitudinal resonance at 600 nm. These features will be analyzed within the theory developed in chapter two and it will be shown that they correspond to resonances in the value of the metamaterial's effective permittivity. Secondly the theoretical results obtained for the linear optical properties will be used to analyze the nonlinear optical properties of the metamaterial. The results will show the strong enhacement of the nonlinear optical response around both plasmonic resonances. This behavior will be verified using the theory developed in chapter two sections 2.2 and 2.4 and through the finite element method. Finally, measurements of the metamaterial's third order nonlinear coefficient will be realized using the z-scan technique around these plasmonic resonances and I will compare the results with those obtained theoretically.

4.1 Effective medium theory for a plasmonic metamaterial.

As previously said in section 1.3, the permittivity of nanorod based metamaterials can be modeled as an anisotropic tensor having the expression shown in equation (2.23) with a permittivity $\varepsilon_{\perp}$ perpendicular to the rod axis and a permittivity $\varepsilon_{\parallel}$ parallel to the rod axis. Both of them are a function of the rod permittivity ε_{in} and the embedding medium ε_{out}. In the case of a gold based nanorod plasmonic metamaterial, ε_{in} corresponds to the permittivity of a metal (Au) and ε_{out} corresponds to the permittivity of a dielectric (in the case of our nanorod metamaterial it is Aluminum oxide (Al_2O_3) and $\varepsilon_{out} = 2.89$). However as a consequence of the nanorods fabrication procedure, the mean free path of electrons travelling inside them is reduced and an additional correction must be added to the bulk gold permittivity described in equation (2.13). Therefore the total permittivity of the nanorods is [1]

$$\varepsilon_{in} = \varepsilon_r = \varepsilon_{Au} + \frac{i\omega_p{}^2\tau(L-R)}{\omega(\omega\tau+i)(\omega\tau R+iL)} \tag{4.1}$$

Where ε_{Au} is the bulk permittivity of gold derived from the equation (2.13), L (=35.7nm) is the mean free path of electrons, R is the effective mean free path of electrons, restricted by the effects of the structure [1] and $\tau = 1/\gamma_{\text{intra}}(\omega, T_e, T_L)$. In this case R is 13nm to fit the measured optical properties of the nanorod array sample analysed. Later I will discuss the consequences of the variation of R. Therefore taking into account the model described in section 2.2 for the permittivity of a metal and equations (2.30) and (2.33), we can calculate the wavelength dependence of the parameters $\varepsilon_{\perp}$ and $\varepsilon_{\parallel}$ for a given filling factor as shown in figure 4.1. As expected from the definition of equation (2.33) and the metal's permittivity behavior in wavelength, the real part of $\varepsilon_{\parallel}$ has values going from positive at shorter wavelengths to

negative at longer wavelengths. On the other hand, $\varepsilon_{\perp}$ is always positive and has a resonance-like behavior at a wavelength around 550 nm.

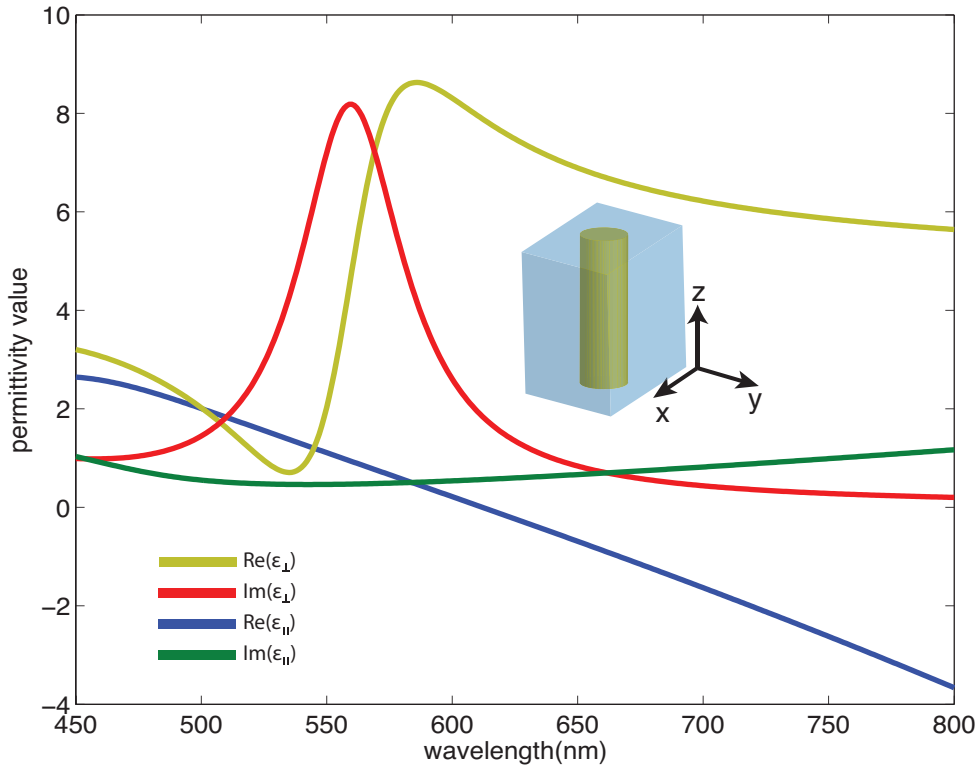

Figure 4.1. Real and imaginary part of ε_{xy} and ε_z calculated using equations (4.1) and theory developed in chapter 2 section 2.3. This is plotted for a filling factor of N=0.25 which is chosen to fit the measured extinction spectra of the nanorod array sample analyzed. The curves are calculated using equations (2.30, 2.33)

This resonance corresponds to the situation when the value of ε_{in} makes the denominator in equation (2.30) close to zero thus obtaining a resonant increase in the magnitude of both real and imaginary parts of $\varepsilon_{\perp}$. Since this resonance is related solely to the value of $\varepsilon_{\perp}$, it corresponds to the optical excitation of electrons in the rod along the x and y direction or in other words perpendicular to the rod axis. This resonance corresponds to the transverse plasmon resonance of the metamaterial and can be observed using either TE or TM polarized optical excitation.

An additional resonance arises under TM polarized excitation and corresponds to an additional resonance in equation (2.33). This resonance occurs when the value of $\varepsilon_{\|} \sim 0$ or ENZ (epsilon-near-zero) regime. Furthermore from equation (2.33) we observe that the resonance increases with increasing angle of incidence as a consequence of the increasing electric field component along z. This resonance corresponds to the longitudinal plasmon resonance of the metamaterial.

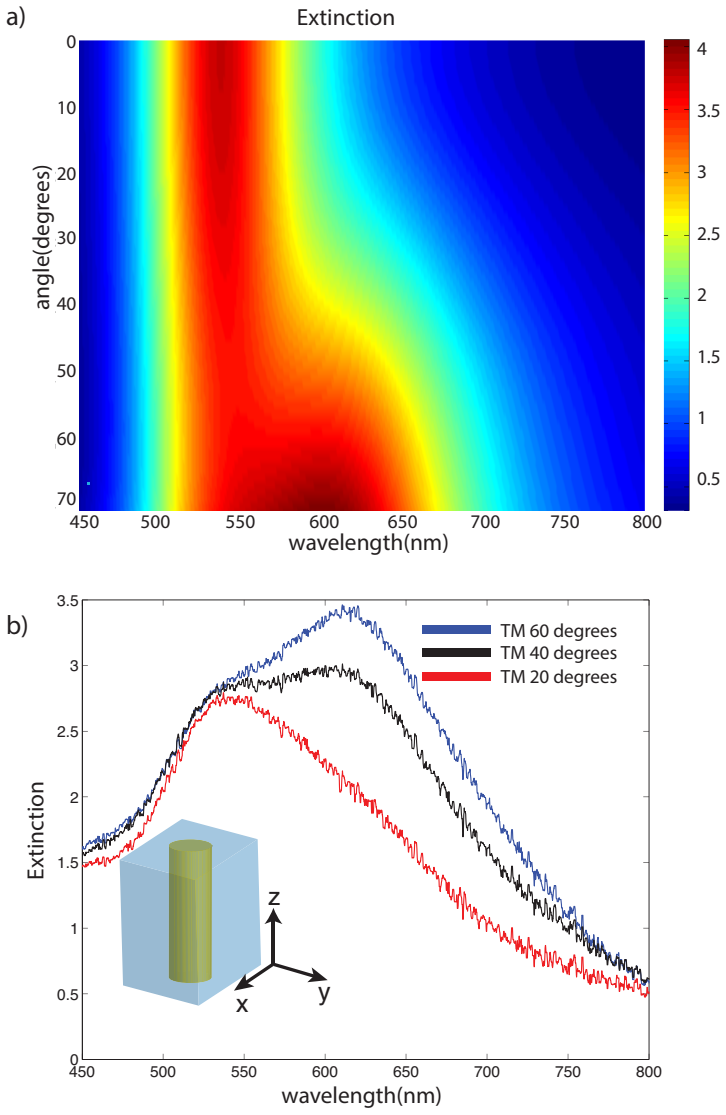

Figure 4.2. (a) Numerically calculated extinction against wavelength and angle of incidence for a layer of 150 nm nanorod metamaterial on glass (SiO_2 n=1.5) calculated using the transfer matrix method. The metamaterial is illuminated with a TM wave, which reveals both the transverse and longitudinal resonance. (b) Measured extinction spectrum at (red) 20 degrees (black) 40 degrees and (blue) 60 degrees. The position of the longitudinal and transverse resonance for the numerical analysis are fitted to match those of the measured spectrum through the parameter N=0.2536

Using equation (2.33) and the transfer matrix method it is possible to compute the extinction of the metamaterial defined as $-\log(T)$ where T is its optical transmission for a TM polarized incident wave. The results are shown in Figure 4.2a and are compared to the experimentally measured extinction spectrum of a nanorod array sample fabricated through a self-assembly technique explained in [1] (Figure 4.2b). At a wavelength of 550 nm and 600 nm we observe the corresponding transverse and longitudinal resonances of the metamaterial for both the theoretically calculated and the experimentally obtained extinction. In the case of TE polarized incident wave only the transverse resonance is excited.

As a final remark, it is worth mentioning that the monotonical increase with angle of incidence in the extinction for the longitudinal plasmon resonance sometimes varies depending on the mean free path of the electrons (R). This effect is not taken into account through the effective medium described here and in section 2.3, as it needs to account for additional longitudinal plasmon resonances instead of only one. This effect is called nonlocality and results from the dependence on the perpendicular wave vector of the permittivity parameter ε_z. The details in the analysis of this behavior can be found in references [2, 3]

4.2 Nonlinear optical properties of a plasmonic metamaterial

The nonlinear optical properties of the metamaterial were modeled using the theory developed in section 2.4. Thus using the transfer matrix method and equation (2.33) together with equation (4.1), the dependence of the absorption coefficient of the metamaterial on the electron temperature is found. Furthermore the stored energy in the metamaterial is dependent on the electron temperature as shown in equation (2.43), where the volume storing the energy corresponds to the rods under the surface being

illuminated by the Gaussian beam. This volume can be calculated through the area at the focus of the beam. This is $V = (\pi(w_0)^2 / (p_{rod})^2)(\pi(d_{rod}/2)^2 h_{rod})$ where the first term in the multiplication corresponds to the number of rods under excitation, and the second term is the volume of a single rod (p_{rod} d_{rod} and h_{rod} are the rod period, diameter and height respectively).

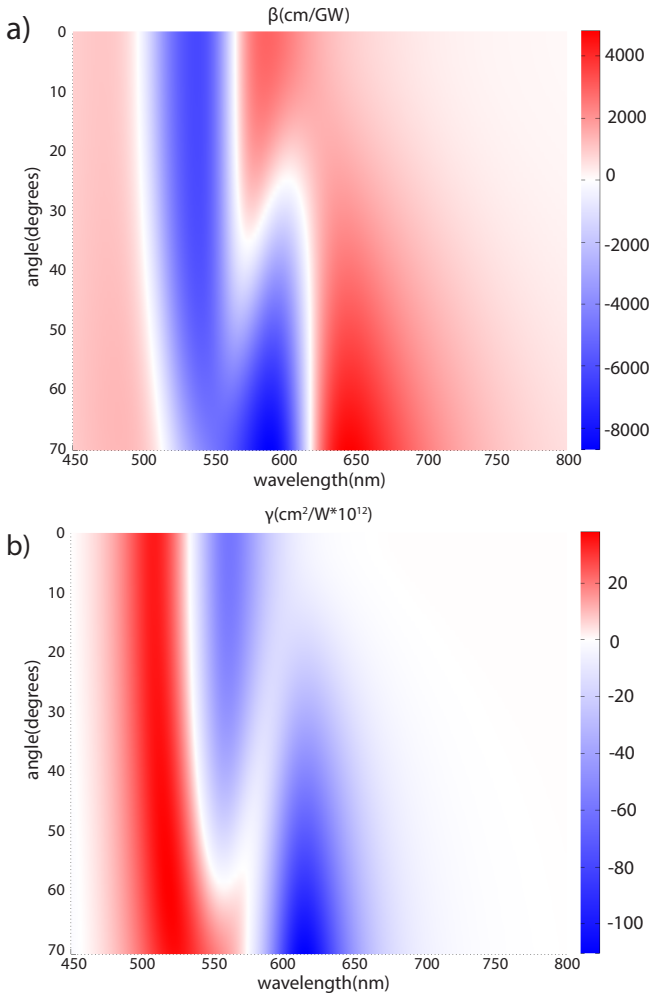

Figure 4.3. (a) nonlinear absorption and (b) nonlinear refraction computed using the theory developed in section 2.2-2.4 together and the transfer matrix method. All the numerical parameters are the same as in figures 4.2 and 4.1.

Therefore the stored energy is dependent on the electron temperature and we can find the zero and first order coefficients of the Taylor's expansion of the metamaterial absorption against the stored energy (A_0 and B_0 of equation (2.41)).

This allows us to find the final stored energy through equation (2.41) and to use equation (2.42) to derive the nonlinear coefficient n_2 of the metamaterial. The results in the case of the nanorods analyzed in the previous section having the linear extinction shown in figure 4.2 are shown in figure 4.3 for both γ and $\beta = 2kn_{2i}$ for a wavelength range of 450 nm -800 nm and angles of incidence from 0-70 degrees respectively. Since the evolution of the metamaterial's absorption is computed taking into account the angle of incidence of the incoming wave, the variation in the absorption takes into account the contribution from both perpendicular and parallel components of the wave's electric field. Thus the implicit anisotropy of the effective $\chi^{(3)}$ for the metamaterial is shown in the angle dependence of both γ and β. In the following section I will analyze the consequence of this anisotropic nature of $\chi^{(3)}$ relating it to the angular dependence of γ and β.

4.3 Analysis of the anisotropy of $\chi^{(3)}$

The effective $\chi^{(3)}$ of the metamaterial is a fourth rank tensor having 81 components. Thus the component in the i direction of the displacement field is given by:

$$D_i = \sum_{j=1,2,3} \varepsilon_{ij}' E_k + \sum_{j,k,l=1,2,3} \chi^{(3)}_{i,j,k,l} E_j E_l E_k \tag{4.2}$$

Which can be written in the following way:

$$D_i = \sum_{j,k,l=1,2,3} (\varepsilon_{ij}' + \chi^{(3)}_{i,j,k,l} E_k E_l) E_j \tag{4.3}$$

Thus the resultant displacement field can be related to an anisotropic linear permittivity having as components the modified linear components (nonlinear anisotropic components):

$$\varepsilon_{ij} = \varepsilon_{ij}' + \sum_{k,l=1,2,3} \chi^{(3)}_{i,j,k,l} E_k E_l \tag{4.4}$$

The prime corresponds to the linear anisotropic component. In the case of diagonal anisotropic materials such as our nanorod array metamaterial, having diagonal linear components $\varepsilon_{xx}' = \varepsilon_{yy}' = \varepsilon_{\perp} \neq \varepsilon_{zz}' = \varepsilon_{\parallel}$, it can be shown through equation (2.35) that the effective linear permittivity can be expressed as [4]:

$$\varepsilon_{eff}(\theta) = \frac{\varepsilon_{xx}'\varepsilon_{zz}'}{\varepsilon_{xx}'\sin^2\theta + \varepsilon_{zz}'\cos^2\theta} \tag{4.5}$$

Where θ is the propagation angle of the wave to which the wave's electric field is dependent through $\vec{E} = E_x\hat{i} + E_z\hat{k} = E_0\cos(\theta)\hat{i} + E_0\sin(\theta)\hat{k}$ ($\hat{i}$ and $\hat{k}$ are unitary vectors along the x and z direction respectively). To understand the dependence of the nonlinear effective permittivity in terms of the anisotropic tensor, we need to use equation (4.4) to replace each linear anisotropic component. This equation allows three angular dependent contributions to the effective nonlinear anisotropic components:

$$\varepsilon_{ij} = \varepsilon_{ij}' + 3E_0{}^2(\chi^{(3)}_{iizz}\sin^2(\theta) + \chi^{(3)}_{iixx}\cos^2(\theta) + \chi^{(3)}_{iixz}\sin(\theta)\cos(\theta)) \tag{4.6}$$

Therefore in the case of the transverse resonance, which has a small variation for both of γ and β with respect to the angle of incidence, we can conclude that in this resonance there is a contribution from both $\chi^{(3)}_{ijxx}$ and $\chi^{(3)}_{ijzz}$ since the sum of these contributions (the second and third term on the right hand side of equation (4.6)) has a vanishing angular dependence. However since the nonlinear coefficients for the longitudinal resonance increase with the angle we can conclude that the main

contribution comes from $\chi^{(3)}_{ijzz}$ (second term on the right hand side of equation (4.6)). Thus the effective nonlinear anisotropic components are:

$$\begin{aligned}\varepsilon_{xx} &= \varepsilon_{xx}' + \chi^{(3)}_{xxzz}\sin^2(\theta){E_0}^2 \\ \varepsilon_{zz} &= \varepsilon_{zz}' + \chi^{(3)}_{zzzz}\sin^2(\theta){E_0}^2\end{aligned} \tag{4.7}$$

Obtaining the effective nonlinear permittivity:

$$\varepsilon_{effnl}(\theta) = \frac{\left(\varepsilon_{xx}' + \chi^{(3)}_{xxzz}\sin^2(\theta){E_0}^2\right)\left(\varepsilon_{zz}' + \chi^{(3)}_{zzzz}\sin^2(\theta){E_0}^2\right)}{\left(\varepsilon_{xx}' + \chi^{(3)}_{xxzz}\sin^2(\theta){E_0}^2\right)\sin^2\theta + \left(\varepsilon_{zz}' + \chi^{(3)}_{zzzz}\sin^2(\theta){E_0}^2\right)\cos^2\theta} \tag{4.8}$$

To a first approximation we can assume that the nonlinear terms in the denominator of equation (4.8) can be negligible in comparison with the sum of the linear terms and thus the denominator remains unchanged. Applying this substitution and expanding the term in the numerator neglecting the terms in order 4 of E_0 we arrive at the following expression:

$$\varepsilon_{effnl}(\theta) = \varepsilon_{eff}(\theta) + \frac{\varepsilon_{eff}(\theta)\sin^2(\theta)\chi^{(3)}_{xxzz}{E_0}^2}{\varepsilon_{xx}'} + \frac{\varepsilon_{eff}(\theta)\sin^2(\theta)\chi^{(3)}_{zzzz}{E_0}^2}{\varepsilon_{zz}'} + \ldots \tag{4.9}$$

We can make an additional approximation assuming again that the nonlinear terms are very small compared to the linear term and thus Snell's law can be written linearly as $\varepsilon_{effnl}(\theta)\sin^2(\theta) = \varepsilon_{eff}(\theta)\sin^2(\theta) = \varepsilon_0\sin^2(\theta_i)$ where ε_0 corresponds to the medium where the incident wave is coming from. Since the value of $\varepsilon_{eff}(\theta)$ is also a function of the angle of incidence related to the Snell's law we can rewrite equation (4.9) as:

$$\varepsilon_{effnl}(\theta_i) = \varepsilon_{eff}(\theta_i) + \frac{\varepsilon_0\sin^2(\theta_i)\chi^{(3)}_{xxzz}{E_0}^2}{\varepsilon_{xx}'} + \frac{\varepsilon_0\sin^2(\theta_i)\chi^{(3)}_{zzzz}{E_0}^2}{\varepsilon_{zz}'} \tag{4.10}$$

As a result we can observe that the linear anisotropy can enhance strongly the effect of the nonlinear anisotropic coefficients in the effective nonlinear permittivity particularly if one of the linear anisotropic coefficients is close to zero. Since the longitudinal resonance occurs within the ENZ (epsilon near zero) regime, equation (4.10) allows the understanding of the large enhancement of the metamaterial's optical nonlinearity obtained at this resonance (Figure 4.3).

4.4 Finite element method modeling of the nonlinear optical properties of a plasmonic metamaterial

The optical properties of the plasmonic metamaterial were simulated using the finite element method [5], which accounts for the shape of the rods. Furthermore, to account as well for the non-homogeneous distribution of the electron temperature in the rods under optical excitation, the two-temperature model defined through equations (2.18) is also solved through the finite element method together with the Maxwell's equations. The coupled solution of these two sets of equations requires a simulation in finite time elements since both sets are time dependent. However since the variations in time of the light's electric field are very fast (in the case of a 550 nm wavelength wave this variation are in the order of the inverse of the frequency which is $1/\omega = 1/ck = \lambda/(2\pi c) = 0.29\,fs$) and the time variation of the two temperature model is in the order of hundreds of femtoseconds, the full simulation of the system will require steps in the order of less than 0.05 fs to describe well the electromagnetic field and a time span of at least 1ps leading to a very time-consuming simulation.

To overcome this problem, Maxwell's equations were solved in the frequency domain for retrieving the power dissipation density over the rod volume $q(\vec{r},\omega,t_0)$ generated at a given time t_0 by the power of a pulse having a Gaussian intensity profile

$I(t) = I_0 \exp(-t^2 / 2{t_d}^2)$ where t_d is the pulse duration. After that, the power dissipation density is introduced as an input to the two-temperature model, which is solved for larger time steps ($\Delta t = 25 fs$) thus during this time period $q(\vec{r},\omega,t_0)$ is assume to be invariant. In terms of the two temperature model (equations 2.18) this can be expressed as:

$$C_e T_e \frac{\partial T_e(r,t)}{\partial t} = \nabla \cdot (K_e \nabla T_e(r,t)) - g(T_e(r,t) - T_L) + q(\vec{r},\omega,t_0) \qquad (4.11)$$

Retrieving for a specific time $t = t_0 + \Delta t$, the electron temperature distribution $T_e(r,t_0 + \Delta t)$. Afterwards, the rod permittivity of the rod is calculated again but this time it will be position dependent as it is dependent on the electron temperature (equation (4.1) together with equations (2.15-2.17). Therefore the permittivity $\varepsilon_{rod}(\omega,T_e(r,t_0 + \Delta t))$ is obtained, which is an input to the maxwell's equations to retrieve the new power dissipation density for the next time step $q(\vec{r},\omega,t_0 + \Delta t)$. This process is repeated until the pulse has passed and the intensity of the pulse is close to zero (About $3t_d$ after the maximum of the pulse intensity).

The electron temperature will relax through electron-phonon coupling within some picoseconds. Therefore, for optical excitation with pulses in the femtosecond regime, the contribution of this coupling is negligible during the time when the optical excitation is occurring, and only equation (4.11) needs to be solved. The variation in the transmission defined as $\Delta T = (T_{nl} - T_0)/T_0$ (where T_{nl} corresponds to the transmission with optical excitation and T_0 corresponds to the linear transmission without optical excitation) is computed using the theory developed in the previous section and the finite

element method developed here. The results are shown in figure 4.4. Both transmission variations are computed assuming an input pulse having energy of 1 pJ.

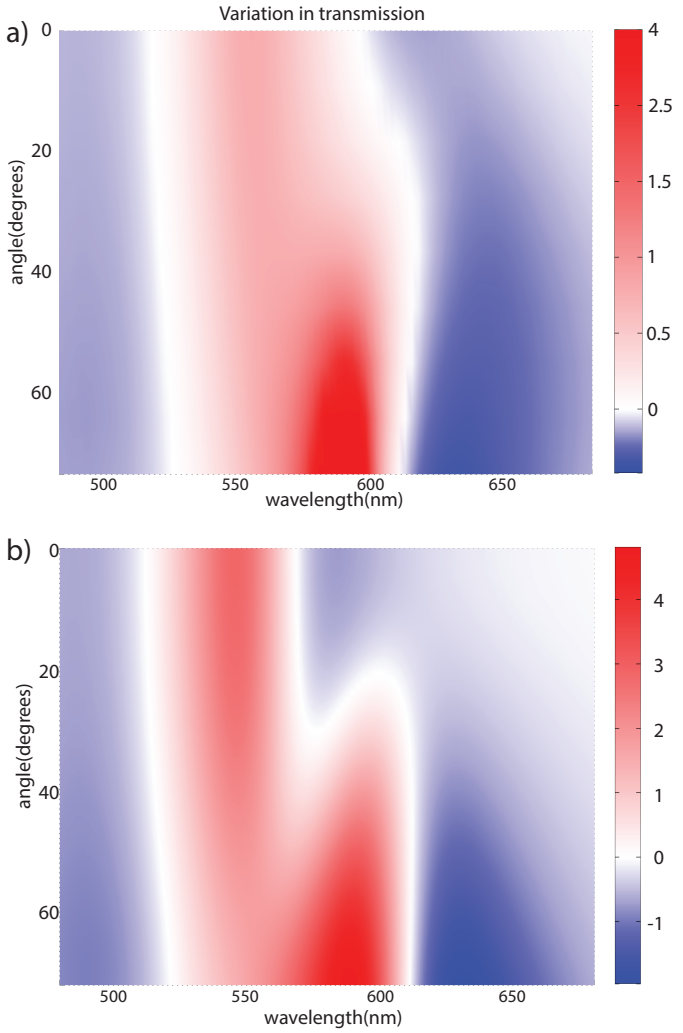

Figure 4.4. (a) variation in the transmission computed using the finite element method coupled to equation (4.10) (b) variation in the transmission computed using the same method used in section 4.2 for computing the nonlinear coefficients.

As expected at both transverse and longitudinal resonance in both cases we have a positive variation in the transmission corresponding to the negative value for beta found in both cases (figure 4.3a). Furthermore for the longitudinal resonance we have also a monotonic increase of the transmission variation. However the value of the achieved transmission variation is higher in FEM than in the case of the effective medium theory

and there is a larger contrast between the transmission variations in and out of resonance.

In summary, the results of the finite element method are similar to those using the effective medium approximation which shows that the simple model developed in the first two sections of this chapter describes well the linear and nonlinear properties of the plasmonic metamaterial.

4.5 Protocol for the z-scan measurement of a nanorod array sample

Gold nanorod samples are generally inhomogeneous as a consequence of the fabrication procedure. Thus when these samples are being scanned through the focus of the Gaussian beam, their transmission is not constant but has some variations depending on the inhomogeneity. Therefore to perform either open or close aperture z-scan in these samples, it is required to perform the following 3 measurements:

1. A z-scan at low intensity power P_0 is performed to retrieve the linear transmission T_0.
2. A z-scan at high intensity with a desired power P_{nl} is performed to retrieve the nonlinear transmission T_{nl}
3. A z-scan again at low intensity is performed to verify that the power applied in step 2 was not enough to damage the sample and change its linear transmission measured in 1.

In the case the verification of step 3 does show that the sample was damaged, then the entire protocol must be repeated again on a different spot on the sample reducing the power until step 3 shows either no or a very small modification in the linear transmission of the sample. Since the nanorod array samples are highly nonlinear they

require very low power thus these measurements must be done with at least 3 times less power than the power used to measured the nonlinearity of gold to prevent damage. Finally T_{nl} is normalized against T_0 to obtain T_{nl}/T_0 which is fitted using the z-scan theoretical curves given in section 3.1 (equation 3.8) and the value of n_2 using a value of I_0 corresponding to the difference in power between the nonlinear and linear transmission ($P_{nl} - P_0$)

4.6 Z-scan results on the plasmonic metamaterial and comparison with theory.

The open and closed aperture measurements were performed at both the resonances of the plasmonic metamaterial (transverse resonance at 550 nm and longitudinal resonance at 600 nm) and at different angles of incidence.

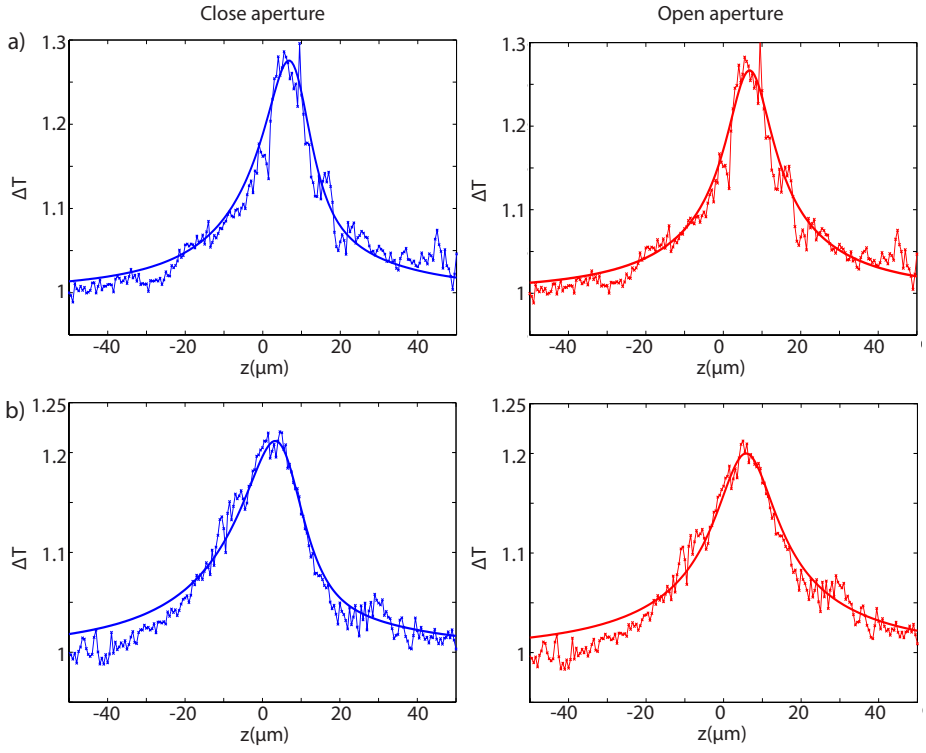

Figure 4.5 a) Close and open aperture z-scan at the transverse resonance of the nanorod array at 550 nm at an angle of 40 degrees and b) at 600 nm at an angle of 60 degrees. All measurements are done using TM polarized light.

The rods are perpendicular to the x-axis defined by the reference frame in Figure 3.4 (At 0 angle of incidence, the rods are aligned with the z-axis). Typical close and open aperture curves for gold nanorods are shown in figure 4.5. A summary of all the coefficients obtained is given in table 4.1 and Figure 4.6 (a-c) shows the variation of the coefficients against the angle of incidence.

For the calculation of the coefficients, the linear absorption of the plasmonic metamaterial needed for the calculation of the effective length, was calculated considering the effective linear absorption using equation (2.37), which increases with the angle of incidence.

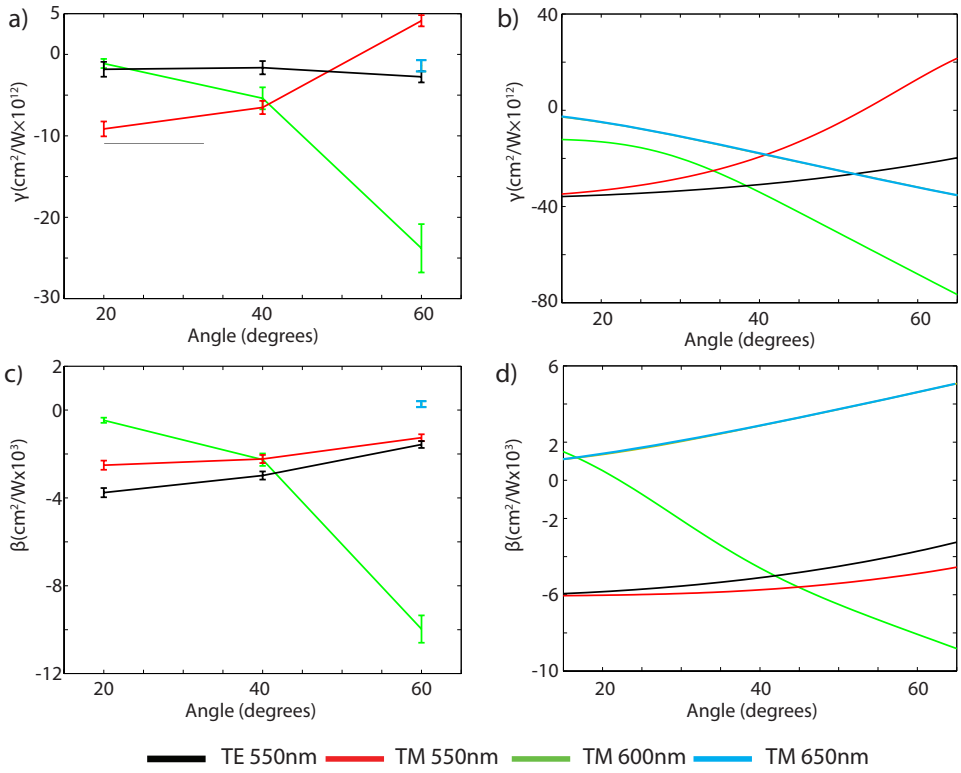

Figure 4.6. (a-b) Nonlinear refraction and (c-d) nonlinear absorption coefficients (a-c) Coefficients measured using the z-scan technique. (b-d) Theoretically calculated. The measurements are done using light (black) TE polarized at 550 nm (Red) TM polarized at 550 nm (green) TM polarized at 600 nm (blue) TM polarized at 650 nm.

Indeed as observed in figure 4.6 (b-d), the behavior predicted by the theory for the nonlinear coefficients in figure 4.3 matches qualitatively the behavior observed through

the z-scan technique. In the case of the transverse resonance we observe that the nonlinear absorption is constant with varying angle of incidence. However the nonlinear refraction decays and changes signs. In the case of the longitudinal resonance we observe the monotonous increase of the nonlinear absorption and refraction with increasing angle

Furthermore, off resonance at longer wavelengths (650 nm), we observe the decrease of the nonlinearity and the shift in the sign. Comparison between figure 4.6 and figure 3.6 reveals the large enhancement obtained between the nonlinear properties of the metamaterial and those of a smooth thin film of gold. Indeed comparing tables 3.1 and 4.1 we have obtained at the wavelength of 550 nm an enhancement in the nonlinear absorption of ~14 and in the nonlinear refraction of ~2 times comparing the largest values found using both polarizations and angles.

T resonance (550nm)						
$\Delta\psi$	$\Delta\phi_0$	Polarization	angle	β (cm/GW)	γ (cm^2/W)	E_p(nJ)
-0.45	-0.05	TE	20	-3762.99±209	(-1.83±0.9)×10^{-12}	0.47
-0.4	-0.05	TE	40	-2980±186	(-1.63±0.8)×10^{-12}	0.47
-0.25	-0.1	TE	60	-1573.4±157	(-2.75±0.68)×10^{-12}	0.47
-0.3	-0.25	TM	20	-2508.66±209	(-9.15±0.9)×10^{-12}	0.47
-0.3	-0.2	TM	40	-2234.22±186	(-6.52±0.8)×10^{-12}	0.47
-0.2	0.15	TM	60	-1258.72±157	(4.13±0.6)×10^{-12}	0.47
L resonance (600nm)						
-0.1	-0.05	TM	20	-467.16±116	(-1.12±0.5)×10^{-12}	0.47
-0.2	-0.1	TM	40	-2259.2±282	(-5.39±1.3)×10^{-12}	0.47
-0.4	-0.2	TM	60	-9967.2±622	(-2.38±0.3)×10^{-11}	0.33
Off the L resonance (650nm)						
0.05	-0.05	TM	60	270.415±135	(-1.40±0.7)×10^{-12}	0.33

Table 4.1 summary of the measurements on the gold nanorod array. In the last measurements the pulse energy was selected to be lower due to possible damage to the sample

In the case of the longitudinal resonance we obtained an enhancement of ~120 in the nonlinear absorption and of ~20 of the nonlinear refraction comparing the largest values obtained which are at an angle of incidence of 60 degrees.

4.7 Conclusion

Plasmonic metamaterials based on nanorod arrays exhibit two plasmonic resonances: transverse plasmon resonance and longitudinal resonance. Through the effective medium theory these resonances have been explained as a consequence of the effective permittivity enhancement occurring when either the value of the permittivity perpendicular to the nanorod axis is resonant or when the value of the permittivity parallel to the nanorod axis is close to zero respectively. Furthermore, it has been shown that through the high optical absorption characteristic of these resonances it is possible to enhance the nonlinear optical response of the system. This behavior has been modeled using the effective medium theory together with the theory described in chapter 2 to model the intensity dependent permittivity of gold. Additionally, the nonlinear absorption and refraction of a gold-nanorod sample was characterized using the z-scan technique described in chapter 3. The theoretical results qualitative describe those obtained experimentally showing the large enhancement of the nonlinearity at both resonances particularly at the longitudinal resonance. Finally, by analyzing the anisotropic nature of the third order nonlinear coefficient, it was shown that the linear properties enhance strongly the response corresponding to the third order nonlinear components of the tensor. In particular, and in agreement with the theoretical and experimental results, when the permittivity parallel to the nanorod axis is close to zero, the nonlinear contribution of the components of the third order nonlinear tensor to the effective nonlinear permittivity is enhanced.

References

[1] R. Atkinson, W. R. Hendren, G. A. Wurtz, W. Dickson, A. V. Zayats, P. Evans, *et al.*, "Anisotropic optical properties of arrays of gold nanorods embedded in alumina," *Physical Review B,* vol. 73, p. 235402, 2006.

[2] J. Elser, V. A. Podolskiy, I. Salakhutdinov, and I. Avrutsky, "Nonlocal effects in effective-medium response of nanolayered metamaterials," *Applied Physics Letters,* vol. 90, pp. 191109-3, 2007.

[3] B. M. Wells, A. V. Zayats, and V. A. Podolskiy, "Nonlocal optics of plasmonic nanowire metamaterials," *Physical Review B,* vol. 89, p. 035111, 2014.

[4] J. J. A. Fleck and M. D. Feit, "Beam propagation in uniaxial anisotropic media," *Journal of the Optical Society of America,* vol. 73, pp. 920-926, 1983.

[5] *Comsol multiphysics 4.3a*, ed, 2014.

Chapter 5: Ultrafast all-optical modulation using hybrid confined modes in plasmonic metamaterials

In this chapter I will present the first application of the high optical nonlinearity of plasmonic metamaterials based on gold nanorods, in particular in using it for ultrafast all-optical modulation. Here the hyperbolic properties of the material are used. It will be shown that in a plasmonic metamaterial waveguide (which I shall refer as meta-waveguide) (i.e. a nanorod waveguide), these properties can be mixed as a consequence of the structure confinement. This leads to the creation of a hybrid mode having both hyperbolic properties and normal properties as it has components parallel and perpendicular to the nanorod axis. Additionally the linear optical properties of this hybrid mode can be changed between normal or hyperbolic when applying an optical excitation to the metamaterial. Finally taking advantage of this property a highly integrated all-optical modulator compatible with silicon photonics will be designed.

5.1 Hybrid anisotropic modes in meta-waveguides.

When light propagates through a waveguide, it propagates in the form of optical eigenmodes as a consequence of the confinement of the structure, which allows only certain eigenvalues for the propagation constant. Assuming that the i-th mode is propagating along the y direction with an electric field $\vec{E}(x,y,z)=\vec{E}_i(x,z)\exp(-\beta_i y+ck_0t)$ inside an isotropic medium waveguide of permittivity ε, it can be proved that all the components of the electric and magnetic field are a function of the components along the propagation direction, which in this case is y [1, 2]. Thus the corresponding wave equations are:

$$\begin{aligned}\frac{\partial^2 E_y^i}{\partial x^2}+\frac{\partial^2 E_y^i}{\partial z^2}+(k_0{}^2\varepsilon)E_y^i=\beta_{Ei}{}^2E_y^i\\ \frac{\partial^2 H_y^j}{\partial x^2}+\frac{\partial^2 H_y^j}{\partial z^2}+(k_0{}^2\varepsilon)H_y^j=\beta_{Hj}{}^2H_y^j\end{aligned} \tag{5.1}$$

Where the super-indexes i and j correspond to the respective modes which in the case of the first equation are called TM (transverse magnetic) modes and in the case of the second equation are called TE (transverse electric) modes. These equations can be also expressed using quantum mechanics notation in the following fashion[3]:

$$\begin{aligned}H\left|E_y^i\right\rangle=\beta_{Ei}{}^2\left|E_y^i\right\rangle\\ H\left|H_y^j\right\rangle=\beta_{Hj}{}^2\left|H_y^j\right\rangle\end{aligned} \tag{5.2}$$

where H defines the operator corresponding to the wave equation at the right hand side of equations (5.1). Therefore $\beta_{Ei}{}^2$ and $\beta_{Hj}{}^2$ are the eigenvalues of the equation. Depending on the boundary conditions of the waveguide, a mode can generally have a small contribution from other modes. This contribution can be added through the addition of a perturbation operator (or coupling operator) W. For example the equation for an hybrid mode composed of two modes j and i, is similar to that of a perturbed two-state system in quantum mechanics:

$$\begin{pmatrix} H & W \\ W & H \end{pmatrix}\begin{pmatrix} |E_y^i\rangle \\ |H_y^j\rangle \end{pmatrix} = \beta_H{}^2 \begin{pmatrix} |E_y^i\rangle \\ |H_y^j\rangle \end{pmatrix} \tag{5.3}$$

Where β_H corresponds to the propagation constant of the hybrid mode. If the corresponding eigenvalues of the coupling operator in this case are assumed to be $W|E_y^i\rangle = A_{ij}|E_y^i\rangle$ and $W|H_y^j\rangle = A_{ij}|H_y^j\rangle$ where A_{ij} is a coupling constant dependent on the boundary conditions, it can be shown that the propagation constant can be expressed as a function of the propagation constants of the composing modes and of the coupling constant [4]:

$$\beta_{H\pm}^2 = \frac{1}{2}(\beta_{Hi}{}^2 + \beta_{Ej}{}^2) \pm \frac{1}{2}\sqrt{(\beta_{Hi}{}^2 - \beta_{Ej}{}^2)^2 + A_{ij}^2} \tag{5.4}$$

The sub-index ± defines the two new hybrid modes composed of the previous modes. It is worth noticing that if $A_{ij} = 0$ or $(\beta_{Hi}{}^2 - \beta_{Ej}{}^2) >> A_{ij}$ then the propagation constant of the hybrid modes remains equivalent to that of the normal modes and both hybrid and normal modes are respectively equal. Therefore only when the $A_{ij} \neq 0$ and when the propagation constants of the two composing modes are similar (or in other words the modes are degenerate), there is a strong coupling between these two. This coupling leads to the deviation of the hybrid mode propagation constant from that of the composing modes.

In the case of a meta-waveguide (plasmonic metamaterial waveguide), the modes are divided into two categories similarly to the propagating plane waves as described in section 2.3: ordinary modes and extraordinary modes. Ordinary modes correspond to modes having $E_z = 0$ and extraordinary modes to those having $E_z \neq 0$. In this context ordinary modes satisfy the wave equation for E_x (or E_y since these are related through

$\nabla \cdot \vec{D} = 0$) whereas extraordinary modes satisfy the wave equation for E_z . Therefore it can be shown [5] that the waves equations for ordinary and extraordinary modes are:

$$\begin{aligned} \frac{\partial^2 E_x^i}{\partial x^2} + \frac{\partial^2 E_x^i}{\partial z^2} + (\frac{\varepsilon_{\|}}{\varepsilon_{\perp}} - 1)\frac{\partial^2 E_z^j}{\partial x \partial z} + ({k_0}^2 \varepsilon_{\perp}) E_x^i &= \beta_{iORD}^2 E_x^i \\ \frac{\partial^2 E_z^j}{\partial x^2} + \frac{\varepsilon_{\|}}{\varepsilon_{\perp}}\frac{\partial^2 E_z^j}{\partial z^2} + ({k_0}^2 \varepsilon_{\|}) E_z^j &= \beta_{jEXT}^2 E_z^j \end{aligned} \tag{5.5}$$

Where β_{iORD}^2 and β_{jEXT}^2 are the eigenvalues corresponding to the ordinary and extraordinary mode. These equations can be expressed as well in quantum mechanics notation as equations (5.2) obtaining:

$$\begin{aligned} H_x \left| E_x^i \right\rangle &= \beta_{iORD}^2 \left| E_x^i \right\rangle \\ H_z \left| E_z^j \right\rangle &= \beta_{jEXT}^2 \left| E_z^j \right\rangle \end{aligned} \tag{5.6}$$

Notice that in this case the operator H_x does not include the term $\partial^2 / \partial x \partial z$ since the field along the z direction for an ordinary mode is zero. However in the case of a coupling between extraordinary and ordinary modes, the resultant hybrid mode allows the inclusion of the term $\partial^2 / \partial x \partial z$ as the field along z is no longer zero. Assuming that $\partial^2 / \partial x \partial z$ corresponds to the operator C having eigenvalues $C \left| E_z^j \right\rangle = B_j \left| E_z^j \right\rangle$, (B_j being the anisotropic coupling constant), the perturbed two-state system equation for an hybrid mode composed of two modes i and j in this case is:

$$\begin{pmatrix} H_x & W + (\varepsilon_{\|} / \varepsilon_{\perp} - 1)C \\ W & H_z \end{pmatrix} \begin{pmatrix} \left| E_x^i \right\rangle \\ \left| E_z^j \right\rangle \end{pmatrix} = {\beta_H}^2 \begin{pmatrix} \left| E_x^i \right\rangle \\ \left| E_z^j \right\rangle \end{pmatrix} \tag{5.7}$$

The eigenvalues are:

$$\beta_{H\pm}^2 = \frac{1}{2}({\beta_{iORD}}^2 + {\beta_{jEXT}}^2) \pm \frac{1}{2}\sqrt{({\beta_{iORD}}^2 - {\beta_{jEXT}}^2)^2 + (\varepsilon_{\|} / \varepsilon_{\perp} - 1)A_{ij}B_j + {A_{ij}}^2} \tag{5.8}$$

Therefore the propagation constant and thus the nature of the hybrid mode depend strongly on the anisotropy of the metamaterial given by $(\varepsilon_{\|} / \varepsilon_{\perp} - 1)$. To appreciate the

consequences of equation (5.8), we will analyze first some of the properties of meta-waveguides which can be easily derived through the analysis of a rectangular meta-waveguide having perfect electric boundary conditions, as illustrated in the inset of Figure 5.1b.

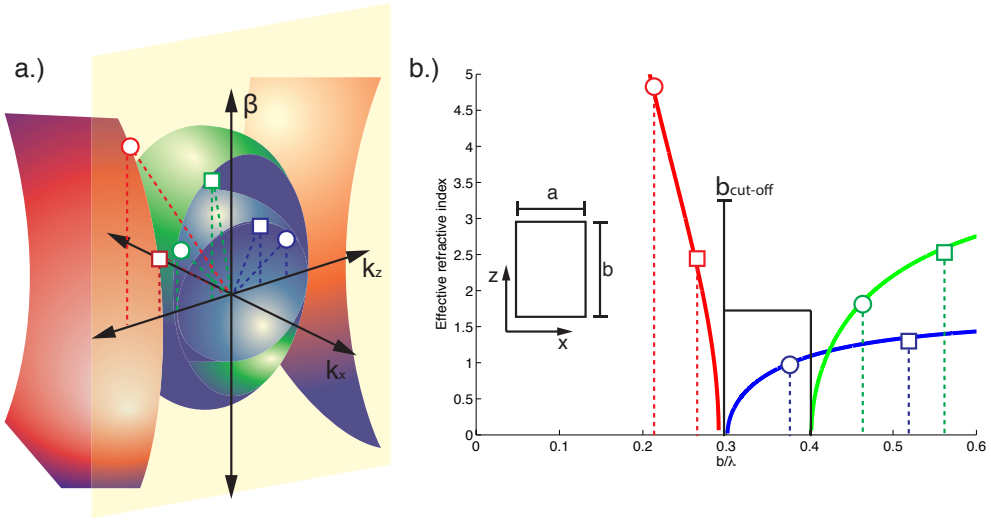

Figure 5.1. a) (blue) normal spherical dispersion (green) Elliptical dispersion (red) Hyperbolic dispersion. b) Effective refractive index against the size b of the waveguide. The colored squares and circles related to the same points in both a) and b). $b_{cut\text{-}off}$ represents the starting point of the modes.

Thus the solutions of equations (5.5) correspond to plane waves with k-vectors satisfying the boundary conditions $k_{nx} = n\pi / a$ and $k_{mz} = m\pi / b$ (n, m being integers corresponding to the ordinary mode i). Substitution of the plane wave solution in equations (5.5) gives:

$$k_{nx}^2 + \beta_{iORD}^2 + k_{mz}^2 = \varepsilon_\perp k_0^2 \tag{5.9}$$

$$k_{n'x}^2 + \beta_{jEXT}^2 + \frac{\varepsilon_{||}}{\varepsilon_\perp} k_{m'z}^2 = \varepsilon_{||} k_0^2 \tag{5.10}$$

Where n' and m' are the integers corresponding to the extraordinary mode j. For elliptical dispersion the anisotropic permittivity values chosen are $\varepsilon_\perp = 9$ and $\varepsilon_{||} = 20$ whereas for hyperbolic dispersion $\varepsilon_{||} = -20$ .The values were chosen arbitrarily

according to typical values obtained for the plasmonic metamaterial at the telecom wavelength (1.55μm) which is our wavelength of interest. Figure 5.1a shows a section (k_x constant) of the different possible surfaces mapped by equations (5.9) and (5.10) in k-space (k_x, β, k_z). The blue surface corresponds to ordinary waves. The green and red surfaces correspond to extraordinary waves in two different cases. For the green surface $\varepsilon_{\parallel} > 0$ and $\varepsilon_{\perp} > 0$ and equation (5.10) maps an ellipsoid. For the red surface $\varepsilon_{\parallel} < 0$ and $\varepsilon_{\perp} > 0$ and equation (5.10) maps a hyperboloid. From these maps it is clear that the dependence of the propagation constant to the dimensions of the waveguide is different in every case. Inspection of equations (5.9) and (5.10) shows that although a variation in k_x (corresponding to a variation in the width) will lead to the same behavior for the propagation constant of both ordinary and extraordinary modes, a variation in k_z will not since in equation (5.10), it is multiplied by the constant $\varepsilon_{\parallel} / \varepsilon_{\perp}$. Figure 5.1b shows the variation of the effective refractive index defined through the propagation constant as $n_{eff} = \beta / k_0$ against the height of the waveguide, which is associated with k_z. It is shown that, although similar behavior is found for the case of the ordinary and extraordinary elliptical mode, the extraordinary hyperbolic mode has a different behavior. In the hyperbolic case, firstly we observe that even for b close to zero it is possible to have a propagating mode with a high propagation constant value. This is evident from the red curve in Figure 5.1b as for a large value of k_z there is still a point having a value for β unlike the other cases. Secondly, for increasing value of b the effective refractive index decreases up to zero in contrast to the other cases where it increases up to the value of the material's refractive index. Therefore for a normal ordinary mode or an elliptic extraordinary mode there is a cut-off value b_{cutoff} which for $b > b_{cutoff}$, the mode propagate through the waveguide (figure 5.1b). In contrast

extraordinary hyperbolic modes have the opposite behavior where there is still a cut-off value b_{cutoff} but the mode can propagate for $b < b_{cutoff}$.

To induce the coupling between these different modes, instead of having our waveguide surrounded by perfect electric boundary conditions, we use dielectric boundary conditions [1, 2]. Therefore numerical simulations of the behavior of the propagation constant in a meta-waveguide surrounded by air ($\varepsilon = 1$) are done to observe the behavior predicted using equation (5.8). These simulations were realized using the finite element method (FEM)[6]. Two cases were analyzed. In the case of elliptical dispersion (Figure 5.2a) it is found that for the given permittivity values, there is a degeneracy of the (n=1,m=2) extraordinary mode and the (1,1) ordinary mode occurring at a height of $\frac{b}{\lambda} = 0.57$. The coupling between these two modes is evidenced from the mode profiles at different heights of the anisotropic waveguide where away from the height of degeneracy, the modes behave as single extraordinary and ordinary modes but close to it the mode profile is a linear combination between the two (mode profiles inside figure 5.2(a,b)). Similar behavior for the propagation constant is found using equation (5.8) together with (5.9) and (5.10) for the same modes ((1,2) extraordinary mode and (1,1) ordinary mode) as shown in Figure 5.2c. In this case the coupling constants were chosen as $A_{12} = B_1 = 0.01$ to fit closely the behavior found in the simulation. The same analysis is done for the hyperbolic case using the finite element method (Figure 5.2b) and theoretically (Figure 5.2d) with $A_{14} = B_1 = 0.01$. In this case the height of degeneracy is found at $\frac{b}{\lambda} = 0.55$ for the (1,4) extraordinary mode and the (1,1) ordinary mode.

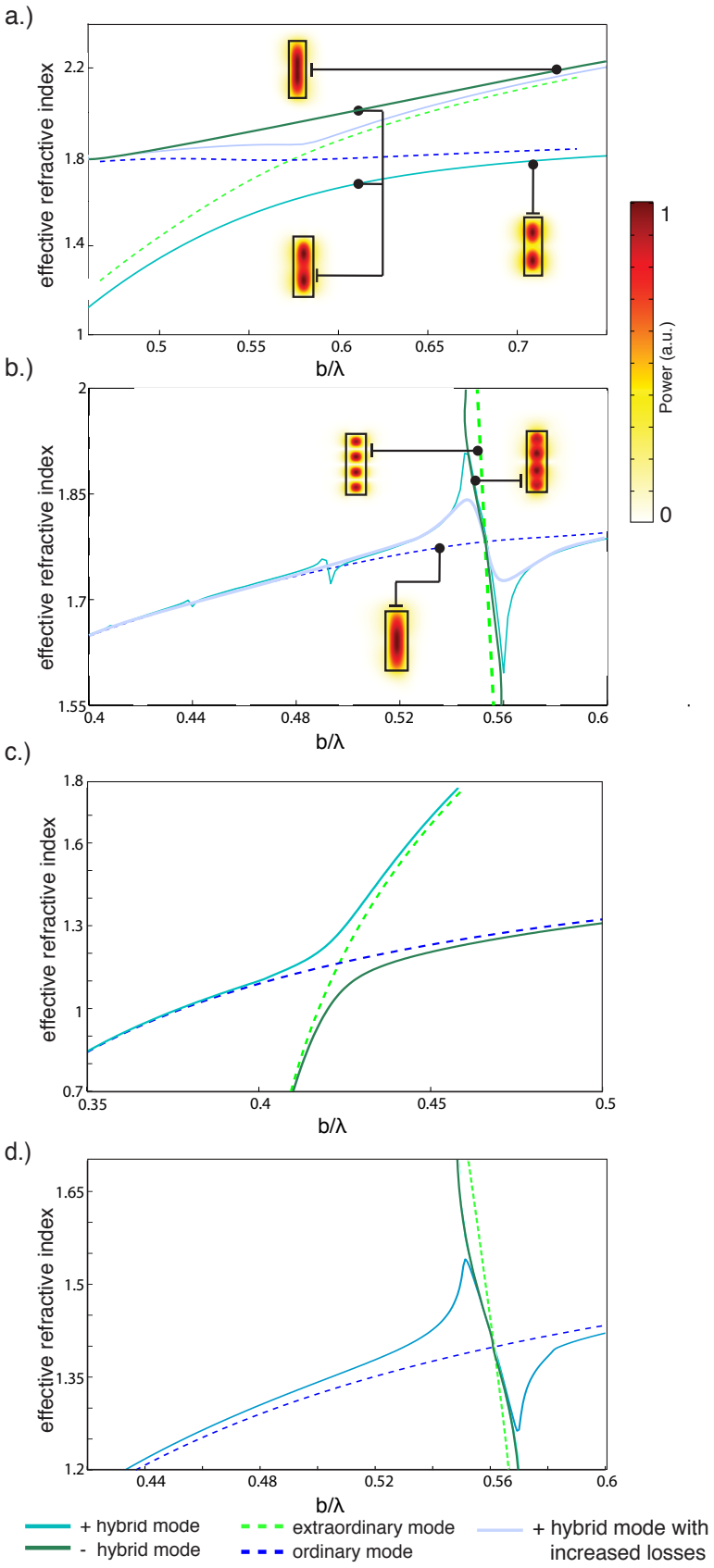

Figure 5.2. Effective refractive index against waveguide height calculated for the (a-c) ordinary mode (n=1,m=1) and extraordinary elliptic mode (n=1,m=2) and the hybrid modes generated. (b-d) ordinary mode (n=1,m=1) and extraordinary hyperbolic mode (n=1,m=4) using finite element method (a-b) using equation 5.8 (b-d) In (a-b) the modes profile are included at the points shown to evidence the coupling.

Interestingly, the hyperbolic condition renders $(\varepsilon_{\parallel}/\varepsilon_{\perp}-1)$ negative and the behavior of the coupling changes leading to the curve shown in Figure 5.2 (b,d).

Additionally it was also analyzed the behavior of the coupling when losses are added to the system as an increase of the imaginary part of either $\varepsilon_{\parallel}$ and $\varepsilon_{\perp}$

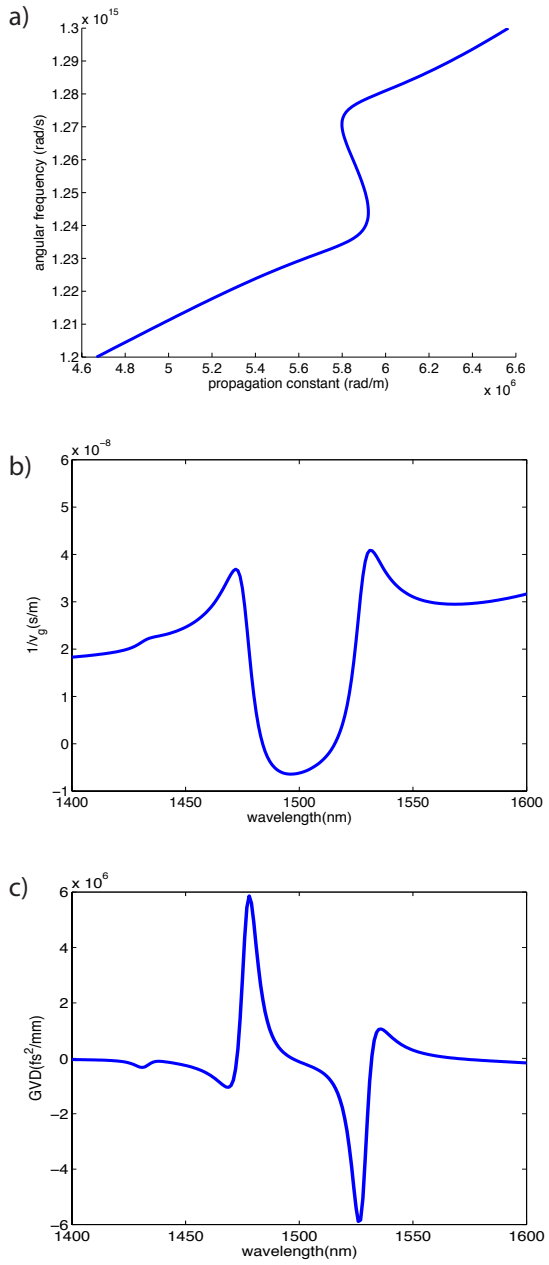

Figure 5.3 a) dispersion of the hybrid hyperbolic mode (angular frequency against wavevector). b) inverse of the group velocity ($1/v_g$) for the dispersion against wavelength. c) Derivative of group velocity dispersion (GVD) defined as $d/d\omega(1/v_g)$

Using the same analysis for two given degenerate modes, it can be found that an increase in the imaginary part of only $\varepsilon_{\perp}$ or both $\varepsilon_{\parallel}$ and $\varepsilon_{\perp}$ breaks the degeneracy of the modes removing the coupling between them as well.

Conversely, when only the imaginary part of $\varepsilon_{\parallel}$ is increased, the degeneracy is not lifted. However using equation 5.8 it can be shown that the propagation constants of the hybrid modes will become the same as those of the original extraordinary and ordinary modes and therefore the coupling between the modes will be reduced. This behavior was also simulated and it is depicted on the gray curves of Figure 5.2a and Figure 5.2b that correspond to a value of $\varepsilon_{\parallel} = 20 + 3i$ and $\varepsilon_{\parallel} = -20 + 3i$ respectively. From the comparison between the curves with and without imaginary part (gray and cyan curves), it is possible to observe how an anisotropic increase in the losses allows the hybrid modes to transform into the original extraordinary and ordinary modes.

This behavior will be used in the following section for the design of an all-optical modulator. Additionally the dependence in wavelength of the particular behavior obtained in the case of the hyperbolic dispersion was analyzed. The obtained dispersion is shown in figure 5.3a. Indeed this dispersion allows regions of group velocity dispersion (GVD), which are negative (Figure 5.3c). Thus the use of these waveguides could be found in applications such as pulse compression or optical signal manipulation.

5.2 Hyperbolic metamaterial all-optical modulator

The coupling demonstrated in equation (5.8) can be done not only between ordinary and extraordinary modes but also between the modes of a normal dielectric waveguide with

the hybrid mode in the meta-waveguide. The basic geometry inducing this coupling is depicted in figure 5.4. The dielectric waveguide, which is a silicon waveguide, is designed to operate in the telecom regime ($\lambda = 1.5\ \mu m$). Therefore its width is 300 nm and is height is 340 nm corresponding to standard fabrication dimensions [7].The meta-waveguide (done using a gold nanorod array) is placed in the top of the slab to reduce the mismatch between the silicon waveguide and the system.

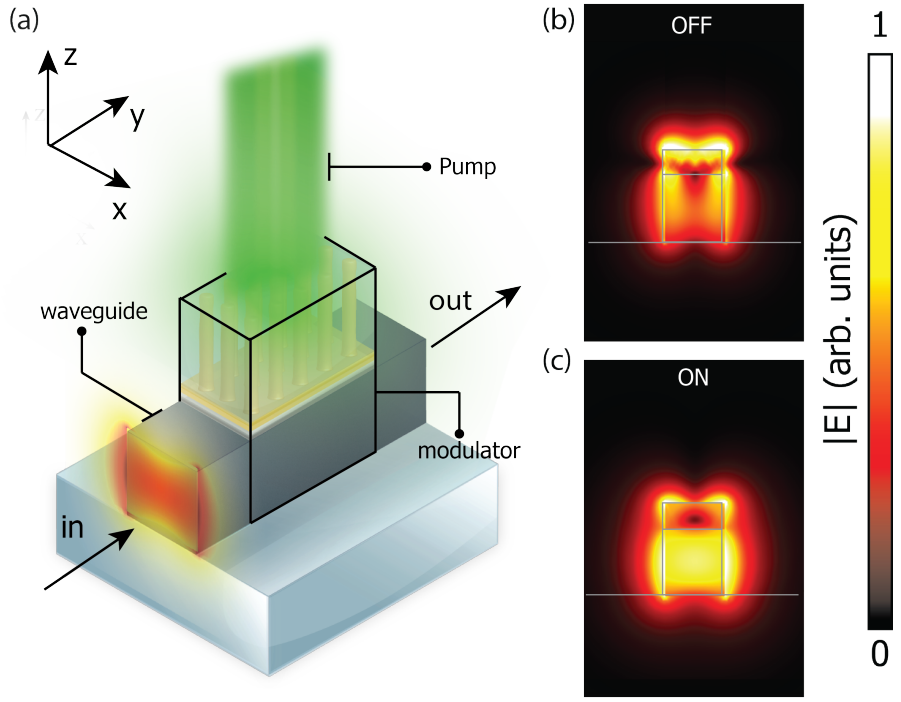

Figure 5.4. (a) Schematic of the modulator. (b) mode profile at the modulator without optical excitation (Te=300 K) and (c) with optical excitation (Te=3000 K).

The combined system composed of the silicon waveguide and the meta-waveguide will be referred to as the modulator. The silicon waveguide has two fundamental modes the first order HE_{x11} polarized in the x direction and the first order HE_{z11} polarized in the z direction. Therefore the mode HE_{x11} will excite ordinary modes in the meta-waveguide whereas the mode HE_{z11} will interact with extraordinary modes in the meta-waveguide. As a consequence the propagation losses of the HE_{z11} mode will be larger than those of

the HE_{x11} since extraordinary modes depend on $\varepsilon_{\parallel}$ which in the case of a gold nanorod array has a larger imaginary part than that of $\varepsilon_{\perp}$ in the telecom regime (i.e figure 4.1). However if the meta-waveguide dimensions are designed to allow the degeneracy of the extraordinary and ordinary modes, the HE_{z11} can couple additionally to ordinary modes and HE_{x11} to extraordinary modes. Thus the propagation losses of the HE_{x11} will increase, while those of the HE_{z11} will remain almost unchanged since ordinary modes depend on $\varepsilon_{\perp}$ which has a smaller imaginary part.

Using the mode-matching technique together with the finite element method to solve for the fields inside the waveguide, it is possible to observe the described behavior. Within this technique the transmission between the modes in the silicon waveguide and the modes in the combined system can be computed through the modified Fresnel formula, taking into account the spatial overlap between the modes [2]

$$T_{ij} = |t_{ij} \cdot t_{ij}^{*}| \frac{\mathrm{Re}(n_j^{\mathrm{mod}})}{n_i^{wg}} \qquad t_{ij} = \frac{2n_i^{wg}}{n_j^{\mathrm{mod}} + n_i^{wg}} \int_S \vec{e}_i^{\,wg}(x,y) \cdot \vec{e}_i^{\,\mathrm{mod}}(x,y) dS \tag{5.11}$$

Where i and j are the eigenmodes of the silicon waveguide and the modulator, respectively, n_j^{mod} is the effective refractive index of the j mode in the modulator, n_i^{wg} is the effective refractive of the i mode in the silicon waveguide and the integral is performed over the modes cross-section. The total transmission through the waveguide/modulator interface with respect to a given eigenmode i of the waveguide consists of the sum of all T_{ij}, corresponding to every eigenmode j supported by the combined system.

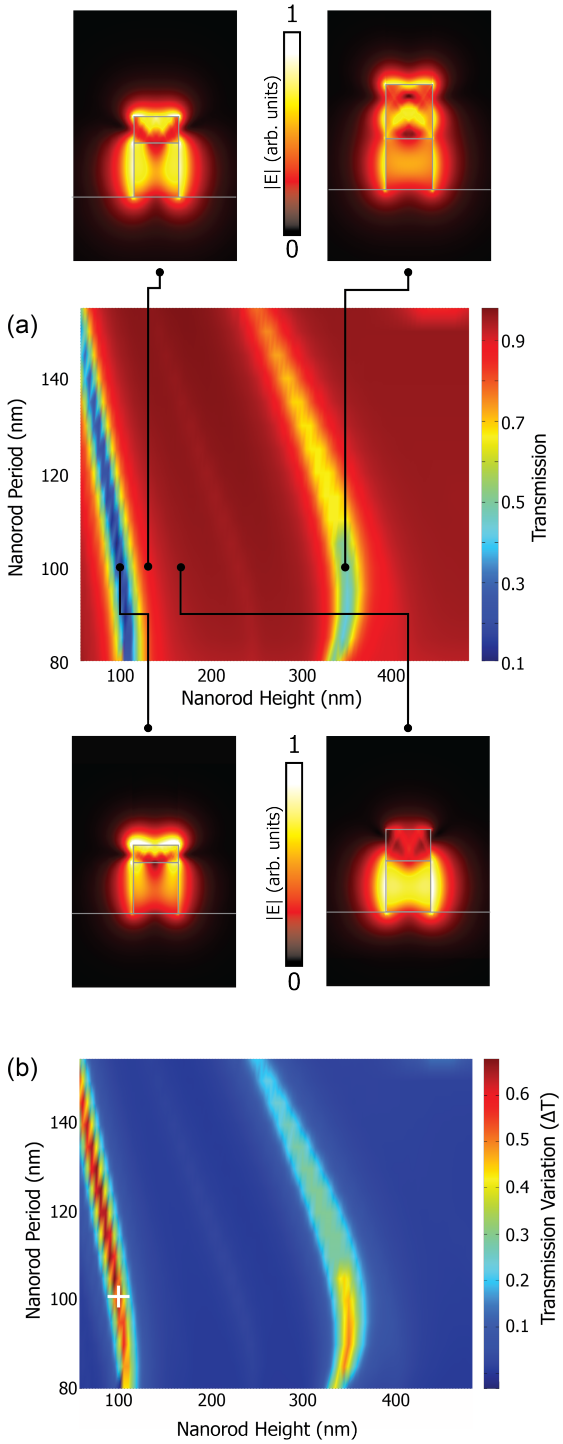

Figure 5.5. a) Transmission computed using the finite element method together with equation 5.11 of the $HE_{11,x}$ mode against the dimensions of the meta-waveguide: nanorod height and period. The diameter is kept constant to 50nm. b) Transmission variation for the $HE_{11,x}$ mode defined as ΔT=T(ON)-T(OFF) against meta-waveguide dimensions. The insets show the mode profiles inside the modulator at each specific point. The white cross in b) shows the point where the 3D calculation for figure 5.6 was done

Using this general formalism (Equation (5.11)), we can estimate the overall transmission HE_{x11} and the HE_{z11} waveguided modes through the modulator's interface

at the operating wavelength of 1.5 μm as a function of meta-waveguide geometry and effective permittivity value. The transmission of the $HE_{11,x}$ mode is shown in the color map in Figure. 5.5(a) as a function of the parametric variables of the metamaterial geometry. A strong sensitivity of the transmission to rod length and spacing is observed with an overall change in transmission from 10% to 95% for different metamaterial parameters in the modulator.

The dimensions where the transmission drops dramatically correspond to those allowing the degeneracy of the ordinary and extraordinary modes in the meta-waveguide. A similar analysis shows more modest transmission values for the $HE_{11,z}$ waveguided mode, only reaching about 40%, but nevertheless also very sensitive to the metamaterial parameters.

As previously said the degeneracy can be lifted through the addition of anisotropic losses in the meta-waveguide. This can be done through its optical excitation. Since the anisotropic permittivity of the meta-waveguide (nanorod-waveguide) is calculated through the equations shown in chapter two, section 2.2-2.3, we have assumed an electron temperature of $T_e(ON) = 3000K$ to compute the transmission of the HE_{x11} when the meta-waveguide is under optical excitation (ON state). The difference in the transmission between the ON state and the OFF state (without optical excitation or $T_e(OFF) = 300K$ as it is shown in Figure 5.5a) is shown in figure 5.5b. Indeed at the dimensions allowing the degeneracy we observe the highest variation in the transmission corresponding to the coupling reduction to the extraordinary mode through the induced anisotropic losses, allowing the HE_{x11} to couple only to ordinary waves.

To determine both the transmission and modulation performance of the proposed device, a 3D numerical modeling was performed on the basis of the optimal modulation geometry (white cross Figure 5.5(b) corresponding to a height of 100 nm and a nanorod period of 100 nm). Calculations were first performed by modeling the nanorod metamaterial within the EMT (effective medium theory) to determine the modulator's switching performance as a function of length. For the considered operating point, the length of the modulator was chosen to be 600 nm as a tradeoff between insertion losses and maximized modulation depth. The transmission of the modulator as the function of the wavelength is plotted in Figure 5.6 (a) in both ON and OFF states.

In agreement with the single interface simulations, the transmission of the device shows a distinct transmission minimum of about 37% at the operating wavelength of 1.5 μm. Figure. 5.6(b,c) shows the plot of the absolute value of the normalized electric field amplitude along the propagation direction for both OFF and ON states. The corresponding mode distribution is depicted in Figure 5.4(b,c), respectively. As predicted analytically, the variation of the mode's spatial confinement in the metamaterial layer as a function of operating conditions is clearly visible. In the ON state, the fundamental mode stays mainly confined to the silicon waveguide decaying exponentially in the nanorod metamaterial. In contrast, the OFF state shows hybridization of the modes, as a significant coupling to extraordinary waves is observed within the metamaterial layer.

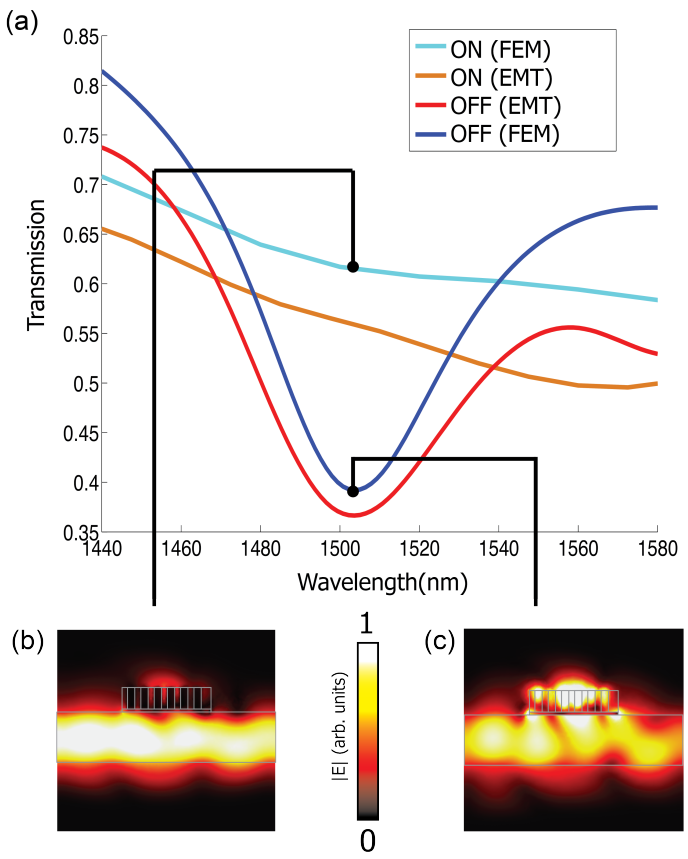

Figure 5.6. a) Transmission calculated using the finite element method for an input $HE_{11,X}$ mode (FEM corresponds to the meta-waveguide modeled as real nanorods with the given dimensions and EMT corresponds to the meta-waveguide modeled using the effective medium approximation described in section 2.3). b) Calculated electric field profile along the modulator for the ON state and c) for the OFF state.

A 50 fs control pulse at a center wavelength of 532 nm provides the optical excitation of the meta-waveguide accessing its transverse resonance, which allows an extinction exceeding 90%. The optical pump (green beam in Figure 5.4a) controls the transmission of the modulator via the change of the temperature-dependent permittivity of the Au nanorods. To compute the total stored energy we use equation (2.43) where the total volume corresponds to that of the metal inside the meta-waveguide. For the considered geometry, an estimated energy of 3.7 pJ is required in order to achieve the 35% modulation (Figure 5.6b). Furthermore, the modulator switching time can be estimated in the framework of the two-temperature model. In the weak excitation regime assumed here, electron-phonon coupling is linear with a decay rate that can be estimated as

$-g/C_e = -2.943\times10^{14} K/s$ for gold, leading to a decay rate of $(C_e/g)\cdot(T(ON)-T(OFF)) = 9.1\,ps$ between ON and OFF states. Since diffusion effects were not accounted for in this estimate, this time corresponds to an upper limit to the practical relaxation time of the device that could, therefore, exceed 100 GHz. This switching speed is well above the typical switching speed of electro-optical modulation [8]. Additionally the insertion losses of our modulator can be calculated by calculating the maximum increase of transmission in the ON state at the desired working wavelength. This was calculated as $-10\log_{10}(0.6)=2.21$ dB.

5.3 Conclusion

In conclusion, through the design of the dimensions of plasmonic metamaterials it is possible to control the optical dispersion of waves propagating within them and as a consequence their optical properties. In particular in the hyperbolic dispersion regime offers several new properties as highly confined hybrid waves, which can be controlled nonlinearly through the optical excitation of the metamaterial and whose properties (such as negative group velocity dispersion) allow new different methods for optical device engineering.

References

[1] J. D. Jackson, *Classical electrodynamics*: Wiley, 1975.

[2] R. E. Collin, *Field Theory of Guided Waves*: Wiley, 1990.

[3] J. D. Joannopoulos, S. G. Johnson, J. N. Winn, and R. D. Meade, *Photonic Crystals: Molding the Flow of Light (Second Edition)*: Princeton University Press, 2011.

[4] B. D. F. L. Claude Cohen-Tannoudji, *Quantum Mechanics Volume 1*: Hermann.

[5] J. J. A. Fleck and M. D. Feit, "Beam propagation in uniaxial anisotropic media," *Journal of the Optical Society of America,* vol. 73, pp. 920-926, 1983.

[6] in *Comsol multiphysics 4.3a*, ed, 2014.

[7] Y. Zhu, X.-J. Xu, Z.-Y. Li, L. Zhou, W.-H. Han, Z.-C. Fan*, et al.*, "High efficiency and broad bandwidth grating coupler between nanophotonic waveguide and fibre," *Chinese Physics B,* vol. 19, p. 5, 2010.

[8] L. Alloatti, D. Korn, R. Palmer, D. Hillerkuss, J. Li, A. Barklund*, et al.*, "42.7 Gbit/s electro-optic modulator in silicon technology," *Optics Express,* vol. 19, pp. 11841-11851, 2011.

Chapter 6: Ultrafast optical modulation using ENZ metamaterials

An ultrafast modulator based on a resonant cavity is designed taking advantage of the ENZ (epsilon near zero) regime, which allows the enhancement of the nonlinear interaction as seen in chapter 4. First I will give a brief introduction of the optical properties of $\varepsilon = 0$ materials making emphasis on the reflectivity. Second I will describe the design of an optical modulator based on a resonant cavity built using two ENZ layers. It will be shown that these layers provide high reflectivity allowing a strong resonant transmission through them, while also introducing low losses. The resultant modulator is highly integrated and low energy consuming.

6.1 Linear optical properties of ε=0 materials.

In the case of materials with $\varepsilon = 0$, the Maxwell's equations for an electromagnetic wave $E(\vec{r},t) = E(\vec{r})\exp(-i\omega t)$ are:

$$\begin{aligned} \nabla \times \vec{E}(r) &= i\omega\mu_0 \vec{H}(\vec{r}) \qquad & \nabla \times \vec{H}(r) &= 0 \\ \nabla \cdot \vec{D}(r) &= 0 & \nabla \cdot \vec{H}(r) &= 0 \end{aligned} \tag{6.1}$$

where μ_0 is the vacuum permeability. Thus the first equation in the right implies that the magnetic field is a constant in space whereas the first equation in the left implies that the electric field is the integral of that constant thus corresponding to a ramp. Using equations (6.1) it can be shown that the relation between the transmitted and reflected electric fields of an $\varepsilon = 0$ layer at normal incidence correspond to[1]:

$$\frac{E_r}{E_0} = \frac{ikd}{ikd-2} \qquad \frac{E_t}{E_0} = \frac{-2\exp(ikd)}{ikd-2} \tag{6.2}$$

which have a dependence on the thickness of the layer (d) as a consequence of the ramp solution for the electric field. In conclusion even if according to Fresnel coefficients a $\varepsilon = 0$ material has reflectivity 1 at its boundary, light can still be transmitted through a small layer. However a $\varepsilon = 0$ material is difficult to design or to find in nature since even if the real part of the permittivity of some materials can be zero, its imaginary part usually is not. As described in chapter 4, by designing the dimensions of the plasmonic metamaterial (nanorod array) it is possible to obtain a material having a permittivity close to $\varepsilon = 0$. In these conditions the material is called an ENZ (epsilon-near-zero) material. For the analysis of the properties of ENZ materials, consider as an example the behavior of the absorption and reflection against the value of the real part of the permttivity computed using the transfer matrix method. The results are shown in Figure 6.1.

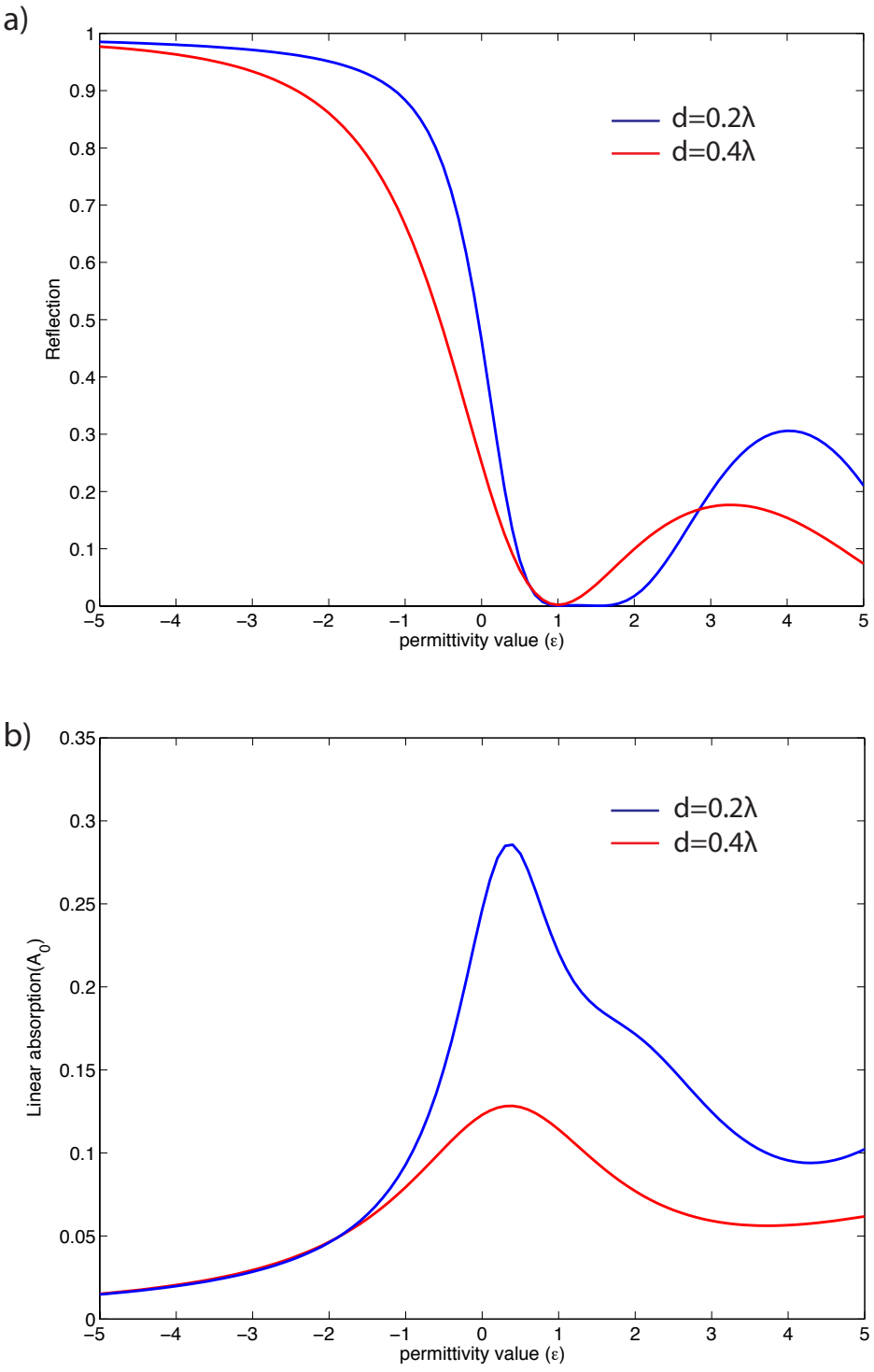

Figure 6.1. a) Reflection and b) Absorption of a layer having real permittivity value ε and an arbitrary imaginary permittivity value of 0.1. These values were calculated for layers having thickness (red) d=0.4/λ (blue) d=0.2/λ with λ the wavelength of the wave coming from air

For values of $\varepsilon \leq 0$, the reflection coefficient is 1, whereas for $\varepsilon > 0$ the reflectivity is low depending on the value of the permittivity around the layer (in this case, air).

Therefore the regime where $\varepsilon \sim 0$ or ENZ regime marks a strong transition between a low and high reflectivity regime exactly as in the case of $\varepsilon = 0$ materials (Figure 6.1a). Thus in the ENZ regime the variation of the reflectivity with respect to the permittivity is the highest ($dR/d\varepsilon$) leading to a high sensitivity of the reflectivity to changes in the effective permittivity. Additionally, close to $\varepsilon \sim 0$ the absorption achieves its largest value, although this decreases with decreasing layer thickness as expected (Figure 6.1b). However, the propagation losses of the wave through a low thickness ENZ layer are smaller. This property will be used in the following section to decrease the insertion losses of the ENZ layers. Hence, according to the theory developed in section 2.4, the nonlinear optical properties of ENZ layers are larger than those belonging to any other dielectric ($\varepsilon > 0$) or metallic ($\varepsilon < 0$) layers, due to the high sensitivity of their optical properties (i.e reflectivity) to the permittivity and their intrinsic high absorption. The high reflectivity and the strong nonlinear properties belonging to the ENZ regime will be used in the following section for the design of a highly integrated all-optical ENZ modulator.

6.2 ENZ all-optical modulator

The high reflectivity of an ENZ layer can be used to construct a resonant optical cavity, which can be optically controlled. The main schematic is shown in figure 6.2. Through the design of the nanorod's dimensions, this cavity can allow the resonant transmission of the fundamental TM mode propagating in a silicon waveguide at the telecom wavelength of 1.55 μm. The multilayer system shown in figure 6.2a is analyzed first by using the transfer matrix method (TMM). The permittivity of the ENZ layer is modeled through the use of equation (2.33). Additionally to minimize further the losses added by the ENZ layers, these are designed with the minimum possible thickness, which corresponds to 1 period of nanorod array or 1 metamaterial unit cell. The value of the

period is chosen arbitrarily to be 90 nm as this is a typical value from the nanorod array fabrication procedure and also from equation (2.33) it can be shown that the variation of this value will just change the variation of the corresponding diameter that ensures the ENZ regime. The system's transmission is plotted against gap and rod diameter in figure 6.3(a).

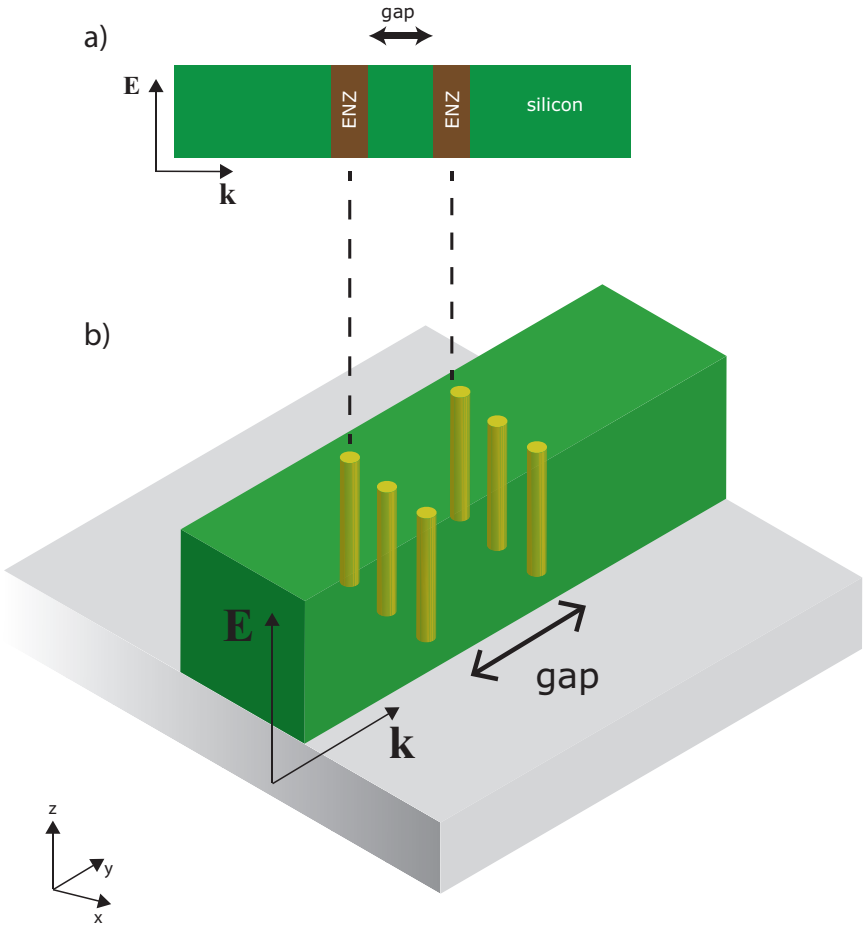

Figure 6.2. Schematic of the ENZ-modulator. a) Two ENZ layers are embedded in a silicon waveguide separated by a gap. The incident mode is TM polarized as shown by the electric field arrow. b) 3D diagram showing the ENZ layer as a single line of nanorods. The silicon waveguide height is 340nm and the width is 300nm (Similar to the silicon waveguide in chapter 5)

At a gap of 70 nm and a diameter of 35nm there is a resonance peak corresponding to the ENZ condition achieved at that diameter. This is further verified by plotting the real part of ε_z against rod diameter using equation (2.30) as seen in figure 6.3c.

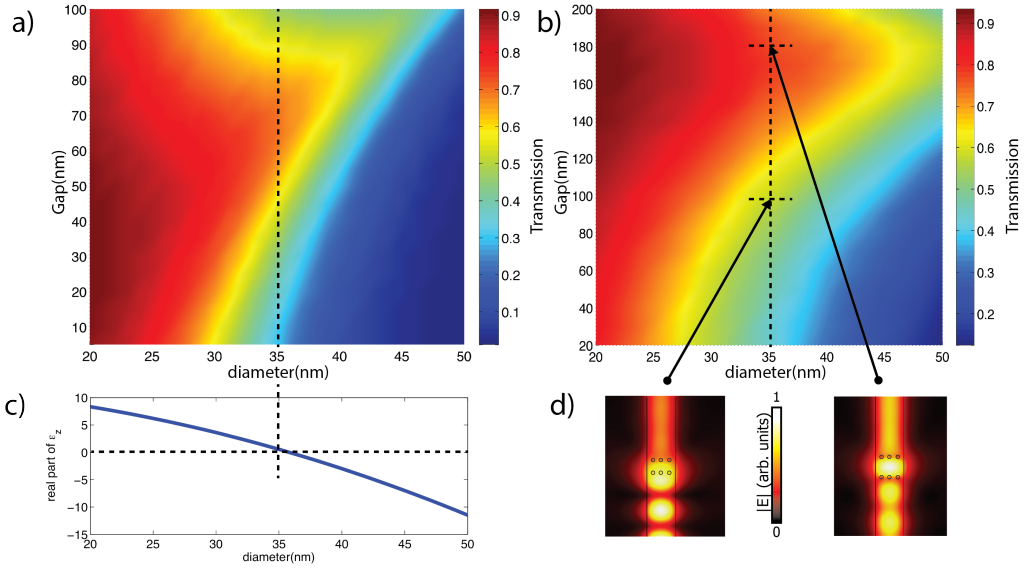

Figure 6.3 Transmission through the cavity against nanorod diameter and cavity gap using a) the transfer matrix method (TTM) and b) full FEM 3D simulation of the schematic shown in figure 5.3b for an input TM polarized mode. c) Real part of ε_z against diameter. d) Field profiles on and off the cavity resonance.

The optical properties of a metamaterial are the result of averaging those of the meta-atoms. Therefore the reduction in ENZ layer thickness performed before for the TMM analysis, corresponds to the creation of a single line of nanorods (figure 6.2b) whose optical response might vary from the average optical response, as the number of meta-atoms is few. In this context to compare the results from theory, the full 3D geometry depicted in figure 6.3b, was simulated using finite element method [2]. As done before the transmission of the fundamental TM mode of a single mode silicon waveguide (height=340nm width=300nm $n_{Si} = 3.48$) is computed against gap and diameter of the rods at a 1.55um wavelength. The results are shown in figure 6.3. Indeed a similar peak appears again for a rod diameter of 35nm and additionally the resonance appears at a gap of 170nm, which is the nanorod period plus the gap derived previously using TTM (transfer matrix method). This corresponds to the distance between the middle of the metamaterial's unit cells, showing that the effective medium theory still holds even for a small number of unit cells. The magnitude of the electric field is plotted along the

silicon waveguide off and on resonance as shown in figure 6.3d. Indeed off resonance the light is almost completely reflected out of the cavity as can be seen from the interference at the waveguide's input. Instead on resonance the light is completely transmitted and inside the cavity there is high electric field magnitude. Similarly as in the case of the modulator shown in chapter 5, to evaluate the nonlinear optical performance of the cavity, its transmission was computed assuming two electron temperatures $T_e(ON)=3000K$ and $T_e(OFF)=300K$ which correspond to the cavity with (ON state) and without optical excitation (OFF state). The results are shown in figure 6.4 where the dimensions of the cavity gap and the nanorods diameter and period are 170 nm, 35 nm and 90 nm corresponding to the dimensions to obtain the resonant peak in figure 6.3a and 6.3b. At the ON state the transmission is decreased since the optical excitation increases the losses inside the ENZ layers increasing their absorption. This is observed on the plot of the electric field magnitude along the waveguide for the ON state. Indeed the high sensibility to the variation in the permittivity at the ENZ regime is observed as the nonlinear variation in the transmission defined as $T(ON)- T(OFF)$ reaches a maximum of 30% (Green curve Figure 6.4).

The performance of the cavity as an all-optical modulator can be characterized additionally in terms of the total energy needed to be absorbed by the cavity to achieve the ON state and also of the insertion losses of the modulator. The first can be calculated as in chapter 5 assuming a uniform electron-temperature across the nanorods composing the ENZ layers using equation (2.43).

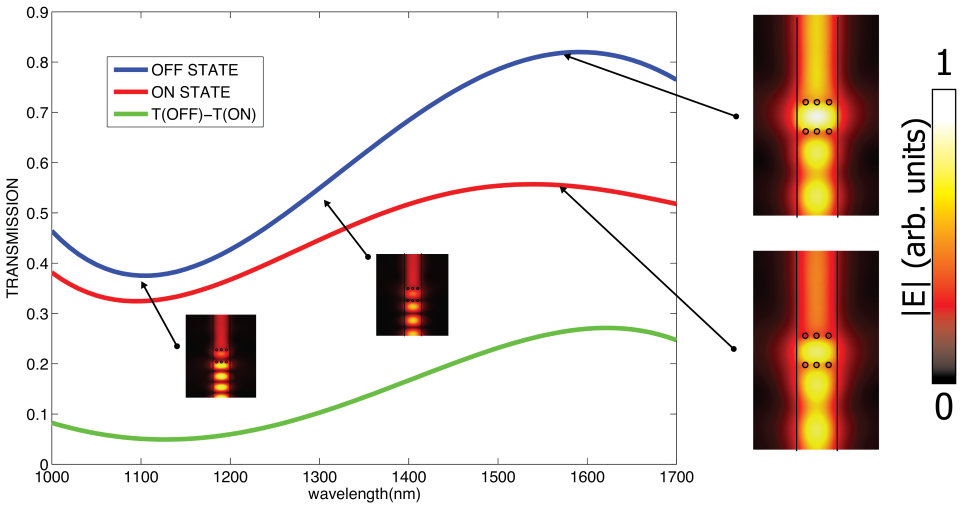

Figure 6.4. Nonlinear optical behavior of the ENZ-modulator. The insets shown, are several field profiles showing the modulator's behavior at different wavelengths. (Red curve) ON state (Blue curve) OFF state (green curve) Difference between the transmission at the OFF and ON state

For the geometry considered a total energy of 600 fJ is required to achieve the 30% modulation in the transmission shown before. Moreover, This energy can be provided through a control pulse at the same wavelength of the signal (1.55 μm) since as previously explained in section 6.1 and in chapter 4, the high absorption of the ENZ layers allows their efficient optical excitation. The insertion losses estimated for this geometry are 0.9dB and the modulation depth of $-10\log_{10}(0.3)/(0.18\ \mu m) = 29.04$ dB/μm. This high value is a consequence of the high confinement of the cavity. In conclusion this modulator exceeds in performance the modulator shown in chapter 4 in both energy requirement and integration.

6.3 Conclusion

In conclusion, the high reflectivity found in ENZ layers together with their enhanced nonlinear optical properties allows the creation of resonant optical systems, which are highly nonlinear and allow all-optical control of light. Furthermore, the integration in silicon waveguide of these layers enables the high integration of the nonlinear cavity.

Moreover, it is remarkable the agreement of the effective medium theory even in the description of systems composed of few meta-atoms. Therefore the results obtained in the modeling of this ENZ cavity may provide the groundwork for the analysis of more complicated systems having a non-uniform distribution of meta-atoms.

References

[1] A. Alù, M. G. Silveirinha, A. Salandrino, and N. Engheta, "Epsilon-near-zero metamaterials and electromagnetic sources: Tailoring the radiation phase pattern," *Physical Review B,* vol. 75, p. 155410, 2007.

[2] *Comsol multiphysics 4.3a*, ed, 2014.

Chapter 7: Conclusion and Outlook

Plasmonic metamaterials based on metallic nanorod arrays support two kinds of plasmon resonances: the transverse plasmon resonance and the longitudinal plasmon resonance. These are accurately characterized using the effective medium theory, which approximates the permittivity of the metamaterial to a diagonal anisotropic permittivity tensor having equivalent components perpendicular to the nanorods ($\varepsilon_{\perp}$) and a different component along the axis of the nanorods ($\varepsilon_{\parallel}$). At both resonances the nonlinear optical properties of the metamaterial are enhanced with respect to those of the composite materials. In the case of the transverse resonance, the enhancement occurs when there is a resonant increase in the real and imaginary part of $\varepsilon_{\perp}$ leading to an increased absorption and optical response of the metamaterial. In the case of the longitudinal resonance the enhancement occurs when $\varepsilon_{\parallel} \sim 0$, increasing the real and imaginary part of the effective permittivity, which is dependent on the angle of incidence (equation 2.33). At this regime, called ENZ (epsilon-near-zero) regime a strong enhancement of the nonlinear optical properties is obtained as a consequence of the metamaterial anisotropy (equation 4.10). This behavior has been verified through the modeling and experimental characterization of a gold-based metallic nanorods array sample having a transverse resonance at 550 nm and a longitudinal resonance at 600 nm. The modeling was performed using effective medium theory and the finite element method by solving Maxwell equations together with the two-temperature model (equation 2.18).

The experimental characterization was done using the z-scan technique at the corresponding plasmonic resonances of the array where an enhancement of about ~120 times over the nonlinear absorption and ~20 times over the nonlinear refraction of a smooth film, is obtained. This analysis can be extended to other metallic nanorod arrays

having plasmonic resonances at different wavelengths or composed of different metals such as aluminium, silver, nickel, copper, etc. However the nonlinear enhancement is highly dependent on the metallic losses since these reduce the strength of the plasmonic resonances. In the future it would be interesting to characterize the nonlinear properties of plasmonic metamaterials based in other metals particularly CMOS-compatible metals such as TiN which has already shown a good properties as a constituent material for metamaterials [1].

Furthermore, as described through the effective medium theory the wavelength and angular dependence of the metamaterial's optical properties is complex and it would be very interesting to perform z-scan measurements at different wavelengths and angles to validate further our model. However z-scan measurements are time consuming, as they require several scans as well as the alignment of the optical parametric amplifier used for the wavelength dependent measurements. In the future, additional measurements will be taken using a completely computer controlled optical parametric amplifier together with the z-scan technique described here which will increase the amount of measurements allowing a broader characterization of the nonlinear properties of the sample. Additionally, pump-probe experiments, in which the changes caused to the sample's spectrum by a high intensity pulse (pump) are recorded, could shed light on other ongoing nonlinear mechanisms occurring in our sample.

In terms of theory, the sample analyzed in this thesis has high losses, which are enough to prevent the visualization of any strong nonlocal effect as described in [2, 3]. Therefore, the model used fits well the linear and nonlinear optical properties observed. However, it would be interesting to understand and model the effects that might occur if

the losses are low enough to approach closely the $\varepsilon = 0$ condition which in theory should increase dramatically the nonlinear optical properties of the sample as underlined in equation (4.10). Nevertheless, the fabrication of samples having low losses is very challenging.

I would like to underline the importance of the ENZ regime in the enhancement of the nonlinear properties with this simple example. Consider an interface between a material having $\varepsilon_1 = 0$ and a material having a very small permittivity close to zero (i.e $\varepsilon_2 = 1 \times 10^{-6}$). The reflectivity at the interface is 1. However, if the permittivity of the first material changes slightly to be $\varepsilon_1 = 1 \times 10^{-6}$, then the reflectivity changes to 0. Therefore with a very small change in the permittivity the reflectivity of the interface has changed 100%. Thus the closest the metamaterial's permittivity is designed to be 0 the largest is the possibility to obtain a theoretically infinite optical nonlinear coefficient.

Furthermore, it is interesting to observe how the effective medium theory has worked well in the understanding of both linear and nonlinear optical properties of the plasmonic metamaterial, especially in the description of a few amounts of meta-atoms such in the case of chapters 5 and 6. Therefore it might be possible to understand still through the effective medium theory some new structures such as metamaterial crystals (for example periodic arrays of metamaterial slabs or meta-waveguides) or disordered meta-atoms. These materials may have new and interesting linear and nonlinear optical properties.

In the future, the experimental optical characterization of the linear and nonlinear properties of the devices shown in chapters 5 and 6 will be realized, the devices will be designed on SOI wafers and the light will be coupled to them using gratings. The results of these experiments will definitely corroborate the properties theoretically described and will allow the birth of different additional applications based on these designs which are the base of a new highly integrated all-optical circuitry, which is capable of operating easily at THz rates.

References

[1] G. V. Naik, J. L. Schroeder, X. Ni, A. V. Kildishev, T. D. Sands, and A. Boltasseva, "Titanium nitride as a plasmonic material for visible and near-infrared wavelengths," *Optical Materials Express,* vol. 2, pp. 478-489, 2012.

[2] J. Elser, V. A. Podolskiy, I. Salakhutdinov, and I. Avrutsky, "Nonlocal effects in effective-medium response of nanolayered metamaterials," *Applied Physics Letters,* vol. 90, pp. 191109-3, 2007.

[3] B. M. Wells, A. V. Zayats, and V. A. Podolskiy, "Nonlocal optics of plasmonic nanowire metamaterials," *Physical Review B,* vol. 89, p. 035111, 2014.

Publications:

Papers

A. D. Neira, G. A. Wurtz, P. Ginzburg, and A. V. Zayats, "Ultrafast all-optic modulation with hyperbolic metamaterial integrated in Si photonic circuitry," Optics Express **22**, 10987-10994 (2014).

A.D Neira, G. A. Wurtz, N, Olivier, M, Nasir and A. V. Zayats, "Eliminating material constraints for nonlinearity with plasmonic metamaterials" (manuscript submitted)

A.D Neira, G. A. Wurtz, W, Dickson, M, Nasir and A. V. Zayats, "Hybrid modes in hyperbolic metamaterial waveguides" (manuscript in preparation)

A.D Neira, G. A. Wurtz, W, Dickson, M, Nasir and A. V. Zayats, "All-optical modulation using epsilon-near-zero metamaterials in silicon waveguide " (manuscript in preparation)

Patents

A. Neira, G. A. Wurtz, A. V. Zayats, "Signal modulation," UK Patent Application No. 1400398.2 (10 January 2014)

A. Neira, G. A. Wurtz, A. V. Zayats, "ENZ modulator," UK Patent Application No. 1412388.9 (14 July 2014)

Conference papers

A. Neira, P. Ginzburg, G. Wurtz, A. V. Zayats, "Design of a nanorod metamaterial for enhanced fast nonlinearities," in *Near-field Optics, Nanophotonics and Related Techniques,* (DONOSTIA - SAN SEBASTIAN,2012).

A. Neira, G. Wurtz, P. Ginzburg, and A. V. Zayats, "Ultrafast metamaterial optical modulator," in *Lasers and Electro-Optics Europe (CLEO EUROPE/IQEC), 2013 Conference on and International Quantum Electronics Conference*, 2013), 1-1.

A. Neira, G. Wurtz, M. Nasir, N. Olivier, A. V. Zayats, "Nonlinear properties of plasmonic metamaterials studied using femtosecond z-scan technique," in *SPIE Photonics Europe 2014 | Photonics, Optics, Lasers, Micro- and Nanotechnologies,* (Brussels, 2014)